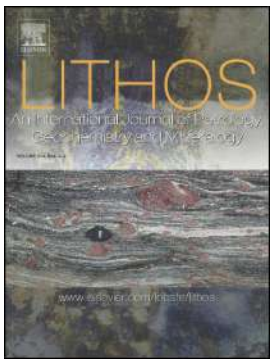

Melt-dunite interactions at 0.5 and 0.7 GPa: experimental constraints on the origin of olivine-rich troctolites

G. Borghini, J.E. Francomme, P. Fumagalli

PII: S0024-4937(18)30343-8
DOI: doi:10.1016/j.lithos.2018.09.022
Reference: LITHOS 4802

To appear in: *LITHOS*

Received date: 27 April 2018
Revised date: 6 September 2018
Accepted date: 17 September 2018

Please cite this article as: G. Borghini, J.E. Francomme, P. Fumagalli , Melt-dunite interactions at 0.5 and 0.7 GPa: experimental constraints on the origin of olivine-rich troctolites. Lithos (2018), doi:10.1016/j.lithos.2018.09.022

Melt-dunite interactions at 0.5 and 0.7 GPa: experimental constraints on the origin of olivine-rich troctolites

Borghini, G., Francomme, J.E., Fumagalli, P.

Dipartimento di Scienze della Terra, via Botticelli 23, 20133 Milano, Italy

Corresponding Author:
Fumagalli Patrizia
Dipartimento di Scienze della Terra « Ardito Desio »
Università degli Studi di Milano
Via Botticelli 23
20133 Milano (Italy)

Email: patrizia.fumagalli@unimi.it

Abstract

Olivine-rich troctolites and dunites are diffuse lithologies at crust-mantle transition of the oceanic lithosphere. Disequilibrium textures coupled to mineral compositions indicate that melt-rock reactions play an important role in their origin. The prevailing view is that olivine-rich troctolites are related to extensive melt impregnation of a precursor mantle dunite.

In order to provide experimental constraints, we performed reactive dissolution and crystallization experiments by juxtaposing three variably evolved MORB-type glasses with a melt-bearing dunite at 1300°C and then cooling to 1150°C at constant pressure (0.5 and 0.7 GPa). Additionally, an isothermal experiment (0.7 GPa, 1250°C) provides a snapshot of olivine-melt reaction after the high-temperature step.

Runs result in glass-bearing gabbro overlain by olivine-rich troctolite (at 0.5 GPa) or dunite (at 0.7 GPa) showing disequilibrium textures comparable with natural occurrences typically related to melt-rock reaction, e.g. embayed and resorbed subhedral olivine with lobate contacts against plagioclase and clinopyroxene, often occurring as large poikiloblasts including rounded olivines. Modal abundance of interstitial phases and mineral chemistry are strongly controlled by the extent of reacting melt infiltrated into the dunite matrix, i.e. the melt/olivine ratio. We found that higher pressure further limits olivine dissolution and results in a lower high-T porosity, decreasing the final abundance of interstitial phases.

Olivine composition is mostly buffered by the starting San Carlos olivine, resulting in high X_{Mg} (0.88-0.90). NiO content decreases at increasing melt/olivine ratio, matching the composition of olivine in natural samples. Remarkably, at very low melt/olivine ratio, NiO can exceed the starting San Carlos value as a result of the increase of Ni olivine-melt partition coefficient during cooling after olivine assimilation in the reacted melt. This might potentially produce high-Ni, at high X_{Mg}, magmatic olivine.

Melt composition affects the chemistry of interstitial minerals that show large compositional variability (anorthite in plagioclase, TiO_2 in clinopyroxene) as a result of local equilibrium driven by trapped melt. Remarkably, mineral co-variation trends (e.g. anorthite in plagioclase vs. olivine X_{Mg}) match those of some natural olivine-rich troctolites occurrences.

Experimental results corroborate and constrain the lead role of melt-rock reactions in the origin of olivine-rich rocks at mantle crust transition in the oceanic lithosphere.

Keywords: Melt-rock reactions, olivine-rich troctolite, oceanic lithosphere, reactive crystallization, experimental petrology

1. Introduction

Olivine-rich troctolites and dunites represent the most primitive rocks of gabbroic sequences in the oceanic crust. They have been documented in oceanic ridge environments (e.g. Lissemberg and Dick, 2008; Godard et al., 2009; Drouin et al., 2009; 2010; Sanfilippo et al., 2013), and in ophiolitic sequences (e.g. Bedard, 1993; Bedard et al., 2000; Borghini et al., 2007; Sanfilippo et al., 2011; Sanfilippo and Tribuzio, 2013). Textural, microstructural and geochemical features of several olivine-rich troctolites are not consistent with fractional crystallization from a primitive MORB (Suhr et al., 2008; Drouin et al., 2009; 2010; Renna and Tribuzio, 2011; Lissenberg et al., 2013; Sanfilippo et al., 2013; Sanfilippo and Tribuzio 2013; Sanfilippo et al, 2014, 2016; Rampone et al., 2016; Renna et al., 2016; Ferrando et al., 2018; Basch et al., 2018). Rather, they indicate that melt-rock reactions play an important role in the formation of the primitive olivine-rich lower oceanic crust (e.g. Rampone et al., 2016; Ferrando et al., 2018, and references therein), as well as in the chemical evolution of MORB (e.g. Collier and Kelemen, 2010; Yang et al., 2013; Paquet et al., 2016; Sanfilippo et al., 2016).

Textures showing partially corroded embayed olivine suggest chemical reactions driven by disequilibrium between a pre-existing olivine matrix and reactive interstitial melts (e.g. Dick et al., 2000; Kvassnes and Grove, 2008; Drouin et al., 2009). In many cases, this is coupled with major element mineral co-variations deviating from pure fractional crystallization with the chemical compositions of interstitial phases far from those typically expected from a low-pressure crystallization (e.g. Lissemberg and Dick, 2008; Suhr et al., 2008; Drouin et al., 2009). Similar features were firstly described in studies on continental

layered intrusions showing that the crystallization of interstitial trapped melt within a cumulus crystal matrix can drastically affect the final mineral composition of cumulate rocks (e.g. Barnes, 1986; Bedard, 1994; Cawthorn, 1996; Charlier et al., 2005; O'Driscoll et al., 2007; Holness et al., 2007).

The interplay between crystallization and melt-olivine reaction has been highlighted for olivine-rich lithologies originated at crust-mantle transition (e.g. Boudier and Nicolas, 1995; Arai and Matsukage, 1996; Arai et al., 1997). On the basis of microstructural and geochemical observations, it has been proposed that olivine-rich troctolites derive from extensive melt impregnation of precursor mantle dunite (e.g. Boudier and Nicolas, 1995; Dijkstra et al., 2003; Droiun et al., 2009, 2010). In this scenario, "replacive" dunite is generated by open-system reactive melt percolation that leads to pyroxene dissolution and olivine crystallization (e.g. Dick, 1977; Quick, 1981; Kelemen et al., 1990, 1995a,b, 2007; Morgan et al., 2008; Dick et al., 2008, 2010; Pirard et al., 2013; Dygert et al., 2016; Rampone et al., 2004, 2008; Rampone and Borghini, 2008). Later, the interaction between dunites and percolating MORB melts via olivine assimilation and concomitant crystallization of interstitial plagioclase and clinopyroxene is inferred to originate olivine-rich hybrid rocks. In the last decades, this interpretation has been invoked for several troctolites from both oceanic (e.g. Suhr et al., 2008; Drouin et al., 2009, 2010; Sanfilippo et al., 2013, 2015, 2016) and ophiolitic settings (Renna and Tribuzio, 2011; Sanfilippo et al., 2011, 2014, 2015; Sanfilippo and Tribuzio, 2013; Rampone et al., 2016; Renna et al., 2016).

One relevant argument for a mantle origin of precursor olivine mostly concerns major element disequilibrium between coexisting minerals (e.g. Suhr et al., 2008; Drouin et al., 2009; Sanfilippo et al., 2013, 2014), coupled with microstructures indicating mantle-like high temperature deformation (e.g. Drouin et al., 2010; Higgie and Tommasi, 2012; Basch et al., 2018) and with correlation to some trace elements (Drouin et al., 2009; Sanfilippo et al.,

2014; Rampone et al., 2016). For example, high X_{Mg} values and NiO content in olivine have been used to support a mantle origin of some troctolites (e.g. Suhr et al., 2008; Drouin et al., 2009; Renna and Tribuzio, 2011; Sanfilippo and Tribuzio, 2013; Sanfilippo et al., 2013), whereas the chemistry of interstitial clinopyroxene (i.e. X_{Mg}, Cr_2O_3 and TiO_2 contents) and plagioclase (anorthite content) have been adopted to discriminate the chemistry of infiltrating melts and/or pressure of crystallization (e.g. Meyer et al., 1989; Ross and Elton, 1997; Coogan et al., 2000a,b; Lissenberg and Dick, 2008; Drouin et al., 2009; Sanfilippo et al., 2013). The hybrid reactive nature of some troctolites has been recently demonstrated by tracing the microstructural and geochemical evolution of olivine matrix (Basch et al., 2018). However, in several case studies, these interpretations are far to be univocal and whether the olivine-rich matrix has magmatic origin or represents mantle dunite relict is still a matter of debate (e.g. Drouin et al., 2009; Rampone et al., 2016).

Several experimental works have been devoted to the role of melt-rock reaction in melt migration through the mantle (Daines and Kholstedt 1993, Lambart et al., 2009; Soustelle et al., 2013; Wang et al., 2013; Pec et al., 2015), reactive dunite formation (Morgan and Liang, 2003, 2005; Beck et al., 2006), and chemical modification of minerals and melts during melt percolation through the lithospheric mantle (Koepke et al., 2009; van den Bleeken et al., 2010, 2011). These isothermal experiments significantly enlarged our understanding of the kinetics, mechanisms and reaction products of basalt-peridotite interactions, focusing on key processes at conditions of the thermal boundary layer where melt migration is strongly affecting both the peridotite matrix and the percolating melts. More recently, the effect of in situ crystallization of reacted melts in a peridotitic matrix has been investigated through step cooling experiments after an isothermal isobaric dissolution stage (Tursack and Liang, 2012; Saper and Liang, 2014). These studies successfully reproduced the formation of dunite-harzburgite and dunite-harzburgite-lherzolite sequences, (Tursack and Liang, 2012), and

hybrid plagioclase-bearing peridotite and plagioclase-bearing wehrlite (Saper and Liang, 2014), widely documented in ultramafic massifs. However, reaction crystallization within an olivine matrix has not yet been experimentally investigated.

In this study, we performed basalt-olivine reaction experiments following a step-cooling path in order to provide experimental constraints to the origin of olivine-rich rocks by reactive dissolution and in situ crystallization within a dunite matrix. Specific aims are to define the role of melt composition on the products of reactive crystallization at two different pressures, 0.5 and 0.7 GPa.

2. Experimental and analytical techniques

We performed six reactive crystallization experiments by juxtaposing a melt-bearing dunite to a layer of powdered MORB glass (Fig. 1a). The charges were first pressurized to 0.5 or 0.7 GPa at 400°C and then run at 1300°C for 24hrs. Melt-olivine reaction couple was step-cooled, at a rate of 10°C/min, down to 1150°C following the temperature-time path shown in Figure 1b. Experimental charges were held at 1150°C, at fixed pressure, for 24 hours to promote crystallization from the interstitial melt. High-porosity melt trap, made of a thin layer of vitreous carbon spheres has been inserted at the top of the capsule and used to promote reactive melt percolation (Van den Bleeken et al., 2010), mostly during the high temperature step. However, as we will discuss below, the absolute amount of melt migrated into the carbon spheres likely plays a minor role in the frame of the aims of this study.

2.1. Starting Material

The compositions of starting olivine and melts are reported in Table 1. The starting

materials for the reacting melts are three synthetic glasses representing variably evolved MORB-type melts (Fig. 2). AH3 and AH6 are two tholeiitic basalts whose phase relations and liquid lines of descent have been experimentally investigated by Husen et al. (2016). AH3 is the most evolved basalt, with X_{Mg} (X_{Mg} = Mg/(Mg + Fe^{tot})) and X_{Ca} (X_{Ca} = Ca/(Ca + Na)) lower than AH6 (AH3: X_{Mg} = 0.58, X_{Ca} = 0.73; AH6: X_{Mg} = 0.62, X_{Ca} = 0.77; Table 1). As the most primitive melt, we used a synthetic glass having the bulk composition of the Hess Deep Rise Basaltic Crust (HDRBC, Gillis et al., 2014). This latter has the highest X_{Mg} and X_{Ca} values, 0.74 and 0.79, respectively (Fig. 2). Its X_{Mg} is close to equilibrium with a mantle olivine (X_{Mg}^{liquid} = 0.75), therefore this melt is expected to be the least reactive.

The dunite layer has been simulated using a powder of San Carlos olivine. In order to avoid inclusions the clearest grains have been hand-picked under binocular, the crystals have been crushed, dried and sieved to 36-64 μm. The final olivine powder was further dried at 600°C for 1h in a horizontal oven in air. Its average composition is reported in Table 1. In order to simulate melt impregnation a small amount of basalt (glass/olivine ratio of about 0.09) has been mixed together with olivine (Fig. 1a). Mixtures of San Carlos olivine and basaltic glasses were stored in closed containers in a 110°C vacuum oven.

2.2. Experimental and analytical techniques

Experiments were carried out at 0.5 and 0.7 GPa (Table 2) in a single-stage piston cylinder at the Laboratorio di Petrologia Sperimentale, Dipartimento di Scienze della Terra "Ardito Desio", University of Milano (Italy), using a salt-pyrex-MgO assembly.

In order to avoid Fe loss toward the noble metal, the graphite-lined platinum capsule technique was applied (Ulmer and Luth, 1991) loading, for each experiment, approximately the same proportions of the following layers: i) basaltic powder, ii) olivine (+ 9% melt)

powder and iii) carbon spheres (Fig. 1a). Salt-Pyrex-MgO assemblies were employed and stored in oven at 110 °C for 24 hours before being placed in the piston-cylinder apparatus. Temperature was measured with Pt-PtRh thermocouple (S-type) with estimated accuracy of ± 5 °C.

Chemical analysis, backscattered electron (BSE) images and X-ray chemical maps were obtained using JEOL 8200 Super Probe at Milan University (Italy). Accelerating voltage of 15 kV was applied for all analysis. All minerals were measured with a beam current of 20 nA and 1 µm beam size. In the isothermal run OM15, we analyzed glass using a beam size of 5 μm in order to prevent alkali loss. Counting time was 30 s for peak and 10 s for background. Compositions of core and rims of selected mineral grains were analyzed. We performed image analysis on X-ray chemical maps obtained with the electron microprobe in EDS and WDS to quantify phase abundances and therefore determine the lithology observed across run products.

3. Results

Table 2 summarizes run conditions and phase assemblages. Five dunite-dissolution and crystallization experiments were conducted by using the step-cooled procedure (Fig. 1b) at 0.5 (OM02 and OM03) and 0.7 GPa (OM20, OM21 and OM22) with three different starting melts. Data from one isothermal experiment at 1250°C and 0.7 GPa (OM15) are also reported in this study to evaluate the results of the melt-olivine reaction after the high-T step that precedes the cooling stage.

3.1. Phase assemblages and textures

The isothermal experiment OM15 (0.7 GPa, 1250°C; Table 2) results in a basaltic glass reservoir at the bottom, a central part made by olivine coexisting with interstitial basaltic glass, replacing the starting melt-dunite matrix, and carbon spheres trapping glass at the top of the capsule (Fig. 3a). The melt-olivine interaction is testified by dissolution textures, such as rather large subhedral crystals (~30 µm to ~100 µm) of olivine showing embayed, lobate, often cusped boundaries (Fig. 3b). Smaller rounded olivines (~2 µm to ~15µm) are also present, suggesting the crystallization of new olivine (Fig. 3a, b). Such textures suggest that olivine has been partially dissolved by the reaction with the starting melt and crystallized from reacted melt.

Run products of step-cooled experiments consist of two-layers samples following the initial geometry: i) glass-bearing olivine-gabbro replacing the initial melt layer (Fig. 1a), ii) olivine-rich layer that replaces the starting dunite (Fig. 3c). This latter is composed of olivine, clinopyroxene and plagioclase in different proportions (Fig. 3d, e, f, g), and traces of vermicular interstitial glass of 2 to 5 µm (Fig. 3h). Representative textural relations within the olivine-rich layer in all step-cooled experiments present similar features at 0.5 and 0.7 GPa for all the starting melts used. Olivine is the dominant phase and occurs both as large subhedral crystals (~30 µm to > 100 µm) and as smaller (< 10 - 15 µm) rounded grains.

Subhedral olivines display either straight rims or lobate curvilinear grain boundaries, these latter indicating partial resorption of olivine by the melt (Fig. 3d-h). Small olivines occur as chadacrysts included in large poikilitic plagioclase and clinopyroxene (Fig. 3e). These textural features of olivine in step-cooled experiments are inherited from the initial high-T stages at 1300-1250°C. Indeed, the texture of isothermal experiment OM15 represents a snapshot of the olivine-melt relation before cooling and in-situ crystallization. Dissolution features are preserved after crystallization in the step-cooled experiments, in which interstitial, vermicular and poikilitic clinopyroxenes and plagioclase replaced the interstitial

melt around embayed and cusped grain boundaries of olivine (Fig. 3d, e, f, g). Plagioclase and clinopyroxene show sharp and straight contacts (Fig. 3f, g), suggesting co-precipitation from reacted interstitial melt (Fig. 3f, g).

The olivine-gabbro contains coarse clinopyroxene, olivine grains, feldspar laths, and relatively large melt portions (Fig. 3c). Plagioclase occurs as large tabular crystals transitional towards a skeletal morphology, likely related to moderate undercooling and slow experimental cooling rate. Intergrowth of olivine and plagioclase is also observed.

3.2. Mineral chemistry of reactive dissolution and crystallization

In the diagrams of figures 4, 5 and 6, mineral compositions are plotted against the distance (d), with d = 0 µm corresponding approximately to the interface between the olivine-gabbro and the olivine-rich layer. Mineral chemistry of olivine, plagioclase, and clinopyroxene are reported in the Supplementary Tables 1, 2 and 3, respectively.

3.2.1. Olivine

Figure 4 shows the X_{Mg} and NiO content of olivine in experiments at 0.5 (a, b) and 0.7 GPa (c, d). At 0.5 GPa, core-to-rim compositional variations are observed in both experiments with AH6 and HDRBC melt (OM02 and OM03, respectively, Table 2). Some cores of olivines from these experiments plot within the compositional range of San Carlos olivine (X_{Mg} = 0.902-0.913), but most of them tend to lower X_{Mg} values, up to X_{Mg} = 0.886 (Fig. 4a). Olivine rims vary towards lower X_{Mg}, with the lowest values (X_{Mg} = 0.860 in OM02; X_{Mg} = 0.886 in OM03) in olivine approaching the gabbro to olivine-rich layer interface (Fig. 4a).

At 0.7 GPa, X_{Mg} values always plot below the compositional range of San Carlos olivine (Fig. 4c). In these experiments, core-to-rim compositional variations are negligible. In

the center of olivine-rich layer (d = 500-2000 µm), X_{Mg} is similar in experiments with AH6 and AH3 melt (OM20, OM21 and OM22), and vary within a rather narrow range 0.890-0.902 (Fig. 4c). Approaching, at the bottom, the gabbro layer and, towards the top, the carbon spheres melt trap, olivine has relatively low X_{Mg} values, up to 0.855 in OM20 (with AH6 melt), and 0.862 in OM22 (with AH3 melt) (Fig. 4c). However, X_{Mg} values decrease is not observed at the top of olivine-rich layer in OM21 (Fig. 4c), in which the melt trap layer was missing (Table 2). Interestingly, data from isothermal experiment OM15 (0.7 GPa, 1250°C) rather match the X_{Mg} variation in olivine documented in step-cooled experiments (Fig. 4c), with X_{Mg} ranging from 0.904 to 0.868 (Fig. 3a).

Olivines resulting from reaction experiments have X_{Mg} values higher than those in equilibrium crystallization experiments on AH6 and AH3 melts (Husen et al., 2016). For example, at 0.7 GPa, olivine in equilibrium crystallization experiments on melt AH6 has X_{Mg} of 0.64 and 0.80 at 1175 and 1225°C, respectively, and olivine from melt AH3 show X_{Mg} of 0.583 and 0.645 at 1150 and 1175°C, respectively (Husen et al., 2016).

NiO content in olivine at 0.5 GPa is systematically lower than the NiO content of San Carlos olivine (NiO = 0.37 wt% ± 0.04, Table 1). The variation of NiO along the olivine-rich layer is similar in experiments with AH6 and HDRBC melt, with rims having lower NiO contents than the cores (Fig. 4b). The highest NiO contents (up to 0.27 wt% in OM02 and 0.32 wt% in OM03) are found in the central portion of olivine-rich layer (d = 600-1200 µm). NiO contents are negligible in olivines within the melt traps (d > 2700 µm for OM20 and OM22 and d > 1400 µm for OM03) and near the gabbro layer (d < 50 to 100 µm) (Fig. 4b), suggesting their complete equilibration with the starting melts, which do not contain nickel (Table 1).

At 0.7 GPa, the variations of NiO content in olivine follow the trends observed in experiments at 0.5 GPa, but in the center of the olivine-rich layer olivine reach or exceed the

NiO content of San Carlos (Fig. 4d). As described above for X_{Mg} value, data from OM15 well mimic those from step-cooled experiments (Fig. 4d), suggesting that most of the compositional variability in olivine has been acquired via olivine dissolution and recrystallization during the high-T step, before the cooling (Fig. 1b).

CaO content in olivine is rather high, overall spanning 0.2–0.4 wt% at both 0.5 and 0.7 GPa (Suppl. Table 1). Such high CaO contents in olivine are usual in high-T experiments and they have been documented in previous similar experimental works (e.g. Morgan & Liang, 2003, 2005; van den Bleeken et al., 2010; Tursak & Liang, 2012; Wang et al., 2013; Saper and Liang, 2014). Cr_2O_3 and TiO_2 contents are very low, generally lower than 0.12 and 0.10 wt%, respectively (Suppl. Table 1).

3.2.2. Plagioclase

Figure 5 displays plagioclase compositional variations along the olivine-rich layer in experiments at 0.5 (a) and 0.7 GPa (b). Anorthite in plagioclase (X_{an} = Ca/(Ca+Na)) from experiments at 0.5 GPa is rather heterogeneous, spanning from 0.585 to 0.719 in OM02 (AH6 melt) and 0.609-0.714 in OM03 (HDRBC melt), with values increasing towards the interface with olivine gabbro (Fig. 5a). No significant differences in plagioclase composition are observed as a function of starting melt compositions (Fig. 5a), which have similar X_{Ca} (AH6, X_{Ca} = 0.77; HDRBC, X_{Ca} = 0.79; Table 1). Except for few analyses in the proximity of the interface with the gabbro layer, plagioclases in experiment with AH6 melt have anorthite contents systematically lower than plagioclases in equilibrium crystallization experiments at 0.4 GPa and temperature of 1150, 1175 and 1200°C from Husen et al. (2016)(Fig. 5a).

At 0.7 GPa, anorthite in plagioclase is influenced by starting melt composition, varying from 0.551 to 0.688 in OM20 (with AH6 melt; X_{Ca} = 0.77), and from 0.448 to 0.613 in OM22 (with AH3 melt; X_{Ca} = 0.73)(Fig. 5b). Analyses on single interstitial plagioclase

reveal high anorthite variability even at the grain scale (Supplementary Fig. 1s). In experiments with AH6 melt, anorthite is not strongly correlated with pressure (Fig. 5a,b). Data from experiments OM20 and OM21 are similar, indicating that the presence of melt trap does not impact on plagioclase composition (Fig. 5b). Only in experiments with AH6 melt, anorthite shows a correlation with distance; we found the highest values in the central part of olivine-rich layer and decreasing values at the top and bottom (Fig. 5b).

The anorthite variability in experiments at 0.7 GPa exceeded towards lower anorthite contents the range defined by composition of plagioclase in equilibrium experiments at same pressure on AH6 and AH3 (Husen et al., 2016) (Fig. 5b).

3.2.3. Clinopyroxene

Clinopyroxenes from the olivine-rich layer in experiments at 0.5 GPa displays large X_{Mg} and TiO_2 variability that is even higher at 0.7 GPa (Fig. 6). At 0.5 GPa, clinopyroxene X_{Mg} varies from 0.869 to 0.897 in OM02 (AH6 melt) and from 0.853-0.901 in OM03 (HDRBC melt), with the highest values in the central part and decreasing values to the top and bottom of olivine-rich layer (Fig. 6a). In experiments at 0.7 GPa, X_{Mg} in clinopyroxene is not related to the starting melt composition and increases going far from the interface with the gabbro layer (Fig. 6c). Run OM20 (AH6 melt) shows the larger X_{Mg} value variability, ranging 0.814-0.896 (Fig. 6c). Melt trap occurrence in the experimental charge does not affect the clinopyroxene composition (Fig. 6c,d).

Overall, clinopyroxene X_{Mg} is higher than those in equilibrium crystallization experiments on AH6 and AH3 melts (Husen et al., 2016) (Fig. 6a,c), except for the lowest values observed in OM20 (AH6 melt) close to the interface with gabbro layer, plotting on or below the X_{Mg} of equilibrium clinopyroxene crystallized at 1225°C (Fig. 6c).

TiO_2 content varies similarly in experiments at 0.5 GPa (TiO_2 = 0.56-1.28; Fig. 6b), in

agreement with the similar TiO_2 content of the two starting melts AH6 and HDRBC (Table 1). Most of values fall within the TiO_2 range defined by clinopyroxene crystallized from AH6 melt in equilibrium experiments at 0.4 GPa and T = 1150-1200°C (Husen et al., 2016) (Fig. 6b). At 0.7 GPa, we found significantly higher TiO_2 contents in clinopyroxene from run OM22 (Fig. 6d), reflecting the higher TiO_2 content of the starting melt AH3 (Table 1). Moreover, this experiment shows extremely high clinopyroxene TiO_2 variability, with unusually high values up to 3.58 wt.% that plot well above the compositions of clinopyroxene from equilibrium crystallization experiments on AH3 melt (Husen et al., 2016) (Fig. 6d). In runs with AH6 melts (OM20 and OM21), TiO_2 contents in clinopyroxene are comparable to those in equilibrium crystallization experiments and tend to decrease going far from the interface with gabbro layer (Fig. 6d). Grain-scale variability in both X_{Mg} and TiO_2 has been evidenced by analyses on single interstitial clinopyroxene from run OM20 (0.7 GPa, AH6; Suppl. Fig. 2s).

Al_2O_3, Na_2O and Cr_2O_3 contents in clinopyroxene from olivine-rich layer are not correlated with the distance from the interface with the gabbro layer. Cr_2O_3 contents are not correlated with pressure; they are generally lower than 0.4 wt.%, with the highest values in the run OM02 (0.5 GPa, AH6, Fig. 7a). Al_2O_3 and Na_2O contents are systematically higher at 0.7 GPa; for examples, in experiments with starting melt AH6, clinopyroxene has Al_2O_3 concentrations varying from 5.42 to 7.72 wt% at 0.5 GPa, and from 6.47 to 10.69 wt% at 0.7 GPa (Fig. 7b). Lowest Al_2O_3 contents are found in run OM03 (0.5 GPa, HDRBC). Relatively high Na_2O contents are observed in clinopyroxene from runs at 0.7 GPa, spanning 0.39-0.88 wt%, as compared with those in experiments at 0.5 GPa (0.15-0.45 wt%; Fig. 7c). Interestingly, at 0.5 GPa the lower Na_2O contents in run OM03 reflect the lower Na_2O contents of HDBRC as compared with melt AH6 (Table 1).

3.3. Phases abundance

Phases abundance in the olivine-rich layer were derived by image analyses combining Mg, Al and Ca X-ray maps. Representative phase maps for two experiments are reported in Figure 8 a,b, together with modal abundances derived for the step-cooled runs. Image analysis indicates that the melt-olivine reactive crystallization produces olivine-rich troctolites at 0.5 GPa and dunites at 0.7 GPa (Fig. 8c).

Although textural evidence, mainly observable in isothermal experiments (olivines with linear boundaries against the melt; Fig. 3b), demonstrates that new olivine crystallized from the reacted melt, its amount cannot be defined by image analysis. As a result, experiments will be discussed in terms of the relative proportions between interstitial phases, i.e. clinopyroxene, plagioclase and glass, and the total amount of olivine.

At 0.5 GPa the modal amount of interstitial phases is 15% and 11% in OM02 (AH6 melt) and OM03 (HDRBC melt), respectively. As pressure increases, at 0.7 GPa, the interstitial phases constitute the 6% of the olivine-rich layer regardless the composition of the starting melt (Fig. 8c). Interestingly, when no melt trap is used (run OM21, Table 2), at the same run conditions (i.e. pressure, temperature path, melt composition and starting melt-olivine ratio) the 3% of interstitial phases is found. Assuming that in both experiments at 0.7 GPa the same amount of newly crystallized olivine is produced, this means that the melt migration from the underlain melt layer upwards is reduced or inhibited when no melt trap is present.

Noteworthy, image analysis on the isothermal experiment OM15 (0.7 GPa, 1250°C, AH6 melt) provides a melt/olivine ratio of 0.09 that is comparable to the proportion between olivine and glass in the starting melt-bearing dunite layer.

4. Discussion

4.1. Textural and chemical constraints on melt/olivine ratio

The isothermal experiment OM15 (0.7 GPa, 1250°C) indicates that during the first high-temperature step i) starting basalt layer is completely melted, ii) olivine and interstitial melt are the stable phases in the olivine-rich layer, and iii) the carbon spheres trap is completely filled by melt (Fig. 3a). As the volume ratio between glass and olivine is equal to the basalt/olivine ratio of the starting melt-dunite matrix (≈ 0.09), we can assume that the volume of melt trapped within the carbon spheres approximately represents the amount of melt migrated upward into the dunite layer from the basalt reservoir. Short duration experiments (20-60 minutes at 1250°C), which will be treated in a separate paper, revealed that the melt trap is rapidly filled by melt. Therefore, after few minutes, melt advection in the capsule is interrupted and the experiments evolved in a closed system. Van den Bleeken et al. (2010) explained this process in their melt-peridotite reaction experiments concluding that after the initial melt "flush" the experimental setup changed to a classic "sandwich" setup made by a reaction couple that is expected to induce chemical gradient. However, also taking into account the low and constant thickness of the melt trap (approximately 0.4 mm), we can assume that it had a minor effect on the phase abundances and distribution, and mineral chemistry variations along the capsule.

Textural features and mineral chemistry of our experiments suggest that melt percolation from the basalt reservoir into the dunite layer is more intense at the melt-dunite interface approximately within the first 200-300 μm, where, in fact, we found the highest variability in olivine chemistry (Fig. 4). This latter is due to higher melt/olivine ratios, enhanced by melt infiltration into the dunite matrix, or element diffusion from the adjacent

melt layer, or likely the combination of the two processes. The very low NiO contents in olivine from the interface, as well as in the proximity of the melt trap (Fig. 4b,d), suggest that the composition of phases at these boundaries is more influenced by the melt chemistry. It is indeed coupled to X_{Mg} decreases in both olivine and clinopyroxene (Fig. 4 and 6).

On the other hand, the melt/olivine ratio in the inner part of the dunite layer seems to be remained at rather constant low values (≈ 0.1). At such melt/olivine ratio, the composition of final olivine, in terms of X_{Mg} and NiO, is only weakly modified by the reaction with the melt (Fig. 4), regardless the composition of the starting melt (Fig. 4).

A sensible effect of experimental pressure on melt/olivine ratio within the olivine layer is observed instead. This is reflected in a lower amount of interstitial phases observed in run products at higher pressure, i.e. 0.7 GPa (Fig. 8c). Assuming that melt migration driven by the porous carbon spheres layer is rapidly exhausted, other processes should act in modifying the melt/olivine ratio at different pressures. At the high temperature step, melt-olivine reaction is controlled by dissolution and re-precipitation. We can therefore assume that, at constant initial melt/olivine ratio and temperature, higher pressures favor re-precipitation rather than dissolution. As a result, before cooling, at higher pressure, we expect a melt-olivine network with lower porosity (i.e. the volume of interstitial melt within the olivine matrix) combined with a lower interconnectivity that limits chemical exchanges. On the contrary, at lower pressure, a higher porosity with larger interconnectivity would enhance melt interactions and chemical homogenization.

At cooling, once the interstitial melt starts crystallizing, the porosity is reduced and the melt/rock ratio progressively decreases. Following the same step-cooled path, due to the positive PT slope of melt-solid equilibria (e.g. Husen et al., 2016), the crystallization of interstitial melt occurs at higher temperature at 0.7 GPa than at 0.5 GPa; the greater extent of crystallization at higher pressure further limits the interconnectivity and chemical

homogenization.

4.2. Reactive crystallization vs. equilibrium crystallization

At 0.7 GPa, the comparison between phases abundance in isothermal and step-cooled experiments indicates that a few amount of new olivine crystallized from the reacted melt during the cooling from 1250°C. In order to infer the phases relations resulting from the reactive crystallization during the cooling, we compare our experimental results with the data from experiments of equilibrium crystallization.

Phase equilibria and melt evolution in basaltic compositions have been broadly investigated (e.g. Grove et al., 1992; Villiger et al., 2004, 2007; Husen et al. 2016). In particular, Husen et al. (2016) performed a large set of equilibrium crystallization experiments to derive the liquid line of descent for 3 tholeiitic basalts, AH6, AH3 and AH5 characterized by a decreasing content of MgO (8.6, 8, and 6.4 wt%, respectively). They documented that, at increasing MgO content of melt, the crystallization of olivine is moved to higher temperature (see Fig. 2 in Husen et al., 2016). Indeed, equilibrium crystallization of melt AH6 at 0.7 and 1225°C results in simultaneously precipitation of clinopyroxene, plagioclase and olivine (Husen et al., 2016).

In the reaction experiments using the same starting melt composition AH6, the assimilation of olivine leads to a relevant increase of MgO in the reacted melt (e.g. up to 14.6 wt% - isothermal experiment OM15, Supplementary Table 4). We expect, therefore, that, by reaction within the olivine-rich layer, olivine is stable along the whole interval of temperature whereas clinopyroxene and plagioclase crystallize concomitantly later. This is supported by poikilitic textures made by small rounded olivine included in clinopyroxene and plagioclase (Fig. 3e,f).

X_{Mg} values of olivine and clinopyroxene in reaction experiments are systematically higher than those resulting from equilibrium crystallization (Fig. 4 and 6), as San Carlos olivine acts as chemical buffer. Within the same experiment, plagioclase shows a broad X_{an} variability (Fig. 5), which resulted by the step-cooled procedure. Previous experimental studies on plagioclase-melt equilibria at dry conditions demonstrated that X_{an} in plagioclase decreases with increasing experimental pressure (e.g. Longhi et al., 1993; Panjasawatwong et al., 1995; Takagi et al., 2005). The same pressure dependence has been observed in experiments on subsolidus phase relations in peridotite compositions (e.g. Falloon and Green, 1998; Borghini et al., 2010, 2011; Fumagalli et al., 2017). We do not observe a straightforward correlation of anorthite content in plagioclase with pressure, likely because it could be overprinted by disequilibrium processes. Furthermore, X_{an} varies well beyond the composition of plagioclase in equilibrium crystallization experiments within the same temperature range, generally showing lower X_{an} (Fig. 5). Higher variability is also observed for clinopyroxene composition (e.g. Al_2O_3, Na_2O and TiO_2; Fig. 7). Similar compositional heterogeneity has been documented in previous melt-rock reaction experiments and have been related to the formation of melt pockets and, as a result, to local equilibria, i.e. different degree of fractionation or different buffering phases adjacent to the trapped melt (e.g. van den Bleeken et al., 2010; Saper and Liang, 2014). Similarly, at the grain scale, our reaction experiments display a significant compositional variability of interstitial phases (Suppl. Fig. 1s and 2s).

The high X_{an} variability in plagioclase and the extreme Ti enrichment in clinopyroxene strongly support that melt pockets within the olivine matrix evolve as a closed system and that the final composition of plagioclase and clinopyroxene is likely affected by trapped melt effect (Fig. 6).

4.3. Effect of melt composition

Melt composition does not affect textural features related to olivine dissolution and re-crystallization. On the other hand, phase abundances produced by different melts show some variability. Although at 0.7 GPa experiments run with AH6 and AH3 melts present comparable modal abundance in the olivine-rich layer, at 0.5 GPa olivine interactions with melt AH6 produced a larger amount of interstitial phases as compared with what observed using the more primitive melt HDRBC (Fig. 8). This reflects the difference in X_{Mg} of the starting melts, rather than the melt SiO_2 content that does not vary significantly (Table 1). Indeed, AH6 and AH3 have closer X_{Mg}, 0.62 and 0.58 respectively, whereas HDRBC has X_{Mg} of 0.74 that is much higher than AH6 (Table 1). A more primitive melt is expected to be less reactive against the olivine, thus reducing the dissolution and the porosity after the initial high-temperature step.

Olivine chemistry within the olivine-rich layer is relatively constant in all runs, without any correlation with the melt composition (Fig. 4). Although NiO in olivine shows a larger variability, this is not systematically correlated with the starting melt composition, rather it is mostly controlled by the melt/olivine ratio (see discussion below). This indicates that for a relatively low melt/olivine ratio, as investigated in this study, the composition of olivine produced by the reaction with melt is widely buffered by the composition of starting San Carlos olivine.

Composition of clinopyroxene is affected by the starting melt, mostly seen in Na_2O and TiO_2 contents (Fig. 7d). In particular, TiO_2 content of reacted interstitial melt cannot increase by olivine dissolution (as olivine contains negligible TiO_2), therefore it is related to the TiO_2 content of the starting melt. This is well documented in experiments at 0.7 GPa, in which the extent of TiO_2 enrichment in clinopyroxene is caused by the relatively high TiO_2 of

starting melt AH3 (Table 1). TiO_2 content is however significantly influenced also by a trapped melt effect because its incompatible behavior let it concentrate in last residual liquid and then almost entirely incorporated in the late crystallizing phase, i.e. clinopyroxene.

Plagioclase composition varies within a similar X_{an} range in experiments at 0.5 GPa with no correlation with starting melt compositions (Fig. 5a). Indeed, although plagioclase-melt partition coefficient for alkalis is function of temperature, pressure, melt composition and water content of the melt (Namur et al., 2012, and references therein), the starting melts AH6 and HDRBC have close X_{Ca} (0.77 and 0.79, respectively, Table 1), and do not affect X_{an} in plagioclase (Fig. 5a). Accordingly, in experiments at 0.7 GPa, lower X_{an} in plagioclase reflects the lower X_{Ca} (0.73) of the melt AH3.

It is worth noting that the effect of starting melt compositions on mineral chemistry operates in combination with local equilibrium and/or melt trapped effect.

4.4. Comparison with natural occurrence

Olivine-rich troctolites and dunites generated by melt-rock reaction experiments at 0.5 and 0.7 GPa show the same textural features documented in olivine-rich troctolite from oceanic lithosphere, as Atlantis Massif (Suhr et al., 2008; Drouin et al., 2009, 2010), and ophiolites from Ligurian Alps (Borghini et al., 2007; Renna and Tribuzio, 2011; Rampone et al., 2016) and Corsica (Sanfilippo and Tribuzio, 2013; Sanfilippo et al., 2015). This strongly reinforces the view that reactive dissolution and in-situ recrystallization play a key role in their origin. However, the high modal olivine interval in our experiments (olivine = 85-97 %) only partially covers the mode of olivine-rich troctolites that often contain olivine abundances lower than 80 % (e.g. Drouin et al., 2009; Renna and Tribuzio, 2011; Sanfilippo et al., 2013; Sanfilippo and Tribuzio, 2013; Basch, 2018). As we have seen, the limited melt flux towards

the starting dunite layer resulted in very low melt/olivine ratios evolving in close system crystallization. This is a critical point of difference between experiments of this work and natural samples. The melt-dunite reaction advocated for the origin of natural troctolites is expected to involve large amounts of melt and/or multiple melt infiltration in open systems, both resulting in a minor effect of chemical buffering by pre-existing dunite solid matrix. This explains the relatively high X_{Mg} in olivine from experiments when compared to X_{Mg} in olivine from many natural olivine-rich troctolites (Fig. 9).

High NiO-olivines: mantle origin or reactive crystallization?

NiO content in olivine, coupled with high X_{Mg} values, have been proposed as constraints on environment of formation of olivine-rich rocks because they enable to distinguish the melt composition, the nature and the extent of reaction processes (e.g. Sanfilippo et al., 2013).

Chemical profiles along experimental charges suggest that NiO in olivine is very sensitive to the melt/olivine ratio. In each experiment we observed a) olivines with very low NiO to almost Ni-free, at the interface with the gabbro-layer and with the carbon spheres, b) olivines with NiO content systematically lower than San Carlos, and c) olivines, at 0.7 GPa, with higher NiO content as compared with the starting San Carlos olivine (Fig. 4).

Olivines with NiO approaching to zero reflect a higher melt/olivine ratio, and as a result a higher buffering effect by the melt is assumed.

At 0.5 GPa, within the olivine layer the amount of interstitial melt produced at the high temperature step, is enough to significantly affect and reduce the NiO content of olivine in the matrix. This is further supported by higher core-rim variations in olivines in these experiments with rims having lower NiO (Fig. 4b).

At 0.7 GPa, olivines have higher NiO, in some cases even exceeding that of the San Carlos olivine (NiO up to 0.47 wt%, Fig. 4d). This occurrence is in agreement with the increase of olivine-melt Ni partition coefficient ($D_{Ni}^{ol/liq}$) as temperature decreases (e.g. Hart and Davis, 1978; Matzen et al., 2003, 2017). Quantitatively we can profit of chemical data in the isothermal experiment at 1250°C, 0.7 GPa (OM15); glass pockets within the olivine-layer contain up to 0.11 wt% (Supplementary Table 4), suggesting that in a melt-bearing olivine-dominated system, i.e. at very low melt/olivine ratio, high temperature mantle olivine dissolution leads to NiO enrichment in the interstitial melt. Considering that in the isothermal experiment we found olivines with NiO up to 0.37 wt%, it results a $D_{Ni}^{ol/liq} \approx 3.36$. At 0.7 GPa, in experiments that have been step cooled down to 1150°C, olivines contain up to 0.47 wt.% NiO. This means a maximum $D_{Ni}^{ol/liq}$ of about $0.47/0.11 \approx 4.27$ which is in agreement with the slope reported experimentally by Matzen et al 2003, constructed only considering the effect of temperature, showing an increase of $D_{Ni}^{ol/liq}$ of approximately 0.8 for a decrease of 100°C (see figure 1b, red line in Matzen et al. 2003).

High-NiO content of olivine in natural olivine-rich rocks is considered an indicator of their mantle origin (e.g. Suhr et al., 2008; Drouin et al., 2009; Sanfilippo et al., 2013). Experimental results of this study indicate that high-NiO olivine, at rather high X_{Mg} ($X_{Mg} > 0.88$), could crystallize from a melt that previously assimilated mantle olivine. Our estimates, based on the highest NiO content of reacted melt at 1250°C (run OM15), suggest a maximum of 30% of olivine assimilation. Interestingly, in a closed system, at a melt/olivine ratio that act as efficient buffer for X_{Mg} in olivine, melt-rock reaction would generate olivine-rich troctolites and dunites consisting of magmatic olivine with high NiO content (and relatively high X_{Mg}) but lacking of mantle-like high-temperature deformation.

In Figure 9, NiO contents in olivine from reaction experiments are compared with data from natural olivine-rich troctolites. The use of Ni-free starting melts in experiments resulted

in NiO content that can reach values much lower than natural olivine (Fig. 9). However, the variability of NiO content shown by experimental data covers the range defined by olivine from natural olivine-rich troctolites supporting the hypothesis of the high NiO content in troctolites can results from interaction between mantle-derived olivine and an impregnating more differentiated basaltic melt (e.g. Suhr et al., 2008, Drouin et al., 2009; Sanfilippo et al., 2013; Renna et al., 2011; Ferrando et al., 2018).

Plagioclase and clinopyroxene chemistry in olivine-rich troctolites: experiments vs. nature

Mineral chemistry of interstitial clinopyroxene (mainly X_{Mg}, Cr_2O_3 and TiO_2 contents) and plagioclase (X_{an}) has been adopted to discriminate the chemistry of infiltrating melts and/or pressure of crystallization.

Figure 10 shows the covariation of X_{Mg} in olivine vs. X_{An} in plagioclase in our experiments compared to data from natural olivine-rich troctolites. Steep trends defined by decreasing X_{an} in plagioclase at rather constant high-X_{Mg} olivine have been documented in some troctolites (e.g. Meyer et al., 1989; Borghini et al., 2007; Sanfilippo et al., 2013; Sanfilippo and Tribuzio, 2013) and in olivine gabbros (e.g. Ross and Elton, 1997). Such correlation has been explained as indicator of moderate pressure of crystallization (e.g. Ross and Elton, 1997; Borghini et al., 2007). Alternatively, relatively low X_{an} in plagioclase in fosteritic olivine-rich rocks has been related to post-cumulus crystallization (e.g. Barnes, 1986; Meyer et al., 1989), or infiltration of Na-rich melts in mantle-derived olivine matrix (e.g. Sanfilippo et al., 2013). Reaction experiments of this study define almost vertical trends, with rather variable X_{an} in plagioclase, which are clearly far from fractional crystallization trends (Fig. 10). However, using the same starting melt composition (AH6), we obtained similar X_{Mg} - X_{an} trends at both 0.5 and 0.7 GPa, thus excluding a pressure influence. On the

contrary, a higher variability towards lower X_{an} in plagioclase requires a Na-enriched impregnating melt (AH3, Table 1).

Interactions between mantle olivine and the moderate evolved basalt AH6 resulted in X_{Mg} - X_{an} trends that are in agreement with what observed in the Erro-Tobbio troctolites (Borghini et al., 2007; Rampone et al., 2016; Basch et al., 2016)(Fig. 10). Recently, Basch (2018), has provided robust evidence, mostly based on microstructural observations and trace element chemistry, of their origin by melt impregnation of a mantle-derived dunite. Our experimental data further support the fundamental role of melt-olivine reaction in creating these rocks. Moreover, they are in good agreement with the sharp decrease in X_{an} of plagioclase at rather constant X_{Mg} of clinopyroxene resulting from reactive crystallization models (Collier and Kelemen, 2010; Sanfilippo et al., 2016).

The compositions of oceanic olivine-rich troctolites show relations between X_{Mg} in olivine and X_{an} in plagioclase that do not significantly differ from fractional crystallization trend (Fig. 10). Sanfilippo et al. (2013) reproduced the compositions of troctolites from Godzilla Megamullion (Parece Vela Basin, Philippines Sea) by applying an AFC model (De Paolo, 1981). Starting from variably evolved basalts, similar to those used in our experiments, they fitted natural data by assuming an open system in which a mantle olivine matrix is replenished by several melt infiltration steps. This suggests that a similar effect would be produced by melt/olivine ratios significantly higher than those adopted in our experiments. Higher volume of infiltrating melt is expected to i) lower the X_{Mg} of reacted olivine, by partially overcome the buffer effect of the olivine matrix, and ii) mitigate the trapped-melt effect narrowing the variability of X_{an} in plagioclase, as well as TiO_2 in clinopyroxene. Remarkably, olivine X_{Mg} vs. plagioclase X_{an} data close to the basalt reservoir in reaction experiments, that simulating higher melt/olivine ratios, follow the trend defined by Pineto troctolites (Fig. 10). Although starting from lower olivine X_{Mg} and higher plagioclase X_{an},

similar trends have been derived from the thermodynamic model of reactive crystallization proposed by Sanfilippo et al. (2016) (Fig. 10).

Despite of similar X_{Mg} values, reaction experiments do not reproduce the high Cr_2O_3 content in clinopyroxene generally observed in oceanic and ophiolitic olivine-rich troctolites (Fig. 7a). Such Cr-rich compositions are significantly higher than those of clinopyroxenes in equilibrium with MORB and are thought to reflect partial dissolution of pre-existing spinel grains in the reacting melts (e.g. Lissenberg and Dick, 2008; Suhr et al., 2008; van den Bleeken et al., 2010; Renna and Tribuzio, 2011). The reaction between low-Cr MORB-like melts, used in our experiments, with olivine alone results in interstitial clinopyroxene with very low Cr_2O_3 content (Fig. 7a), indicating the important role of melt-spinel reaction in buffering the final clinopyroxene composition.

TiO_2 content in clinopyroxene is mostly controlled by the melt chemistry, because of slow diffusion of Ti (e.g. van den Bleeken et al., 2010). Relatively high TiO_2 content have been documented in vermicular clinopyroxene from Erro-Tobbio troctolites (Fig. 7d) and ascribed to trapped melt effect (Borghini and Rampone, 2007). Experimental results of this study reveal that the extent of such Ti-enrichment by trapped melt is significantly enhanced by the very low melt/olivine ratio, as indicated by impregnated dunites resulted from our experimental at 0.7 GPa. Higher melt/olivine ratio in olivine-rich troctolites, therefore, could explain the relatively lower TiO_2 content in clinopyroxene in experiments at 0.5 GPa, as well as, in natural samples (Fig. 7d).

High Al_2O_3 contents in clinopyroxene of experiments reflect the crystallization at high pressure; Al_2O_3 contents higher than 6 wt.% have been observed in high-pressure experiments of MORB crystallization (e.g. Bender et al., 1978; Stolper et al., 1980) and melt-rock reaction (e.g. Tursack and Liang, 2012; Saper and Liang, 2014). Crystallization experiments on AH6 basalt by Husen et al. (2016) provide equilibrium clinopyroxene with average Al_2O_3 contents

varying 5.08-5.51 and 7.01-8.87 wt.%, at 0.4 (1200-1150°C) and 0.7 (1225-1150°C) GPa, respectively. These are in good agreement with the composition of experimental clinopyroxenes of this study (Fig. 7b). On the other hand, natural olivine-rich troctolites display clinopyroxenes with systematic lower Al_2O_3 content that might suggest crystallization at pressure lower than 0.5 GPa or, alternatively, might be related to spinel dissolution and/or the extent of reaction (e.g. Saper and Liang, 2014).

The Na_2O content in clinopyroxene from natural olivine-rich troctolites varies within the range defined by our reaction experiments (Fig. 7c), where it is positively correlated with pressure. Remarkably, several data from ophiolitic settings (Erro-Tobbio, Borghini and Rampone, 2007; Rampone et al., 2016; Internal Liguride Unit, Renna and Tribuzio, 2011; Pineto, Corsica, Sanfilippo and Tribuzio, 2013) plot at relatively high Na_2O content (> 0.6 wt%), together with experimental data at 0.7 GPa (Fig. 7c). However, our experiments at 0.5 GPa have revealed a strong correlation of Na_2O with melt composition (Fig. 7c), so that high Na_2O content in clinopyroxene could be related to a Na enriched composition of impregnating melts.

5. Concluding Remarks

We performed basalt-olivine reaction experiments at 0.5 and 0.7 GPa following a step-cooling path (from 1300 to 1150°C) in order to experimentally constrain the origin of olivine-rich rocks by reactive dissolution and in situ crystallization.

At fixed temperature path, a higher pressure in experimental charges results in lower melt/olivine ratio, and, as a consequence, a final lower abundance of interstitial phases, i.e. plagioclase and clinopyroxene. Lower melt/olivine ratio limits the interconnectivity of the melt/solid network reducing chemical homogenization and thus triggering trapped melt effect

on mineral chemistry.

Regardless the composition of reacting melts, at low melt/olivine ratio, X_{Mg} values of olivine are constant and relatively high (0.88-0.90), due to San Carlos olivine acting as chemical buffer. Olivine NiO content is sensitive to melt/olivine ratio, showing systematically lower contents with respect to San Carlos olivine at 0.5 GPa. However, at 0.7 GPa, olivines have higher NiO contents, also exceeding San Carlos olivine value as results of cooling after olivine assimilation in reacted melt. Remarkably, olivine-rich troctolites and dunites can consist of magmatic olivine with high NiO content lacking of mantle-like high-temperature deformation. Experimental data covers the range defined by olivine from natural olivine-rich troctolites supporting their origin from interaction between mantle-derived olivine and an impregnating more differentiated basaltic melt.

The composition of interstitial phases (plagioclase and clinopyroxene) is mostly controlled by the combined effect of reacting melt composition and local equilibria or trapped melt effect. We do not observe a straightforward correlation of anorthite content in plagiolcase with pressure. Clinopyroxene from reaction experiments have much higher Al_2O_3 and lower Cr_2O_3 contents than those in natural samples. This likely highlights the role of spinel dissolution during reaction, although the influence of relatively high pressure of experiments cannot be excluded.

Interactions between mantle olivine and moderate evolved basalts result in high variability of X_{an} at constant forsterite content in olivine, as documented in some olivine–rich troctolites from ophiolitic massifs. Although the experiments of this study do not cover the entire range of critical parameters, such as low pressure and high melt/olivine ratio, they well reproduced textural and some mineral compositional features described in olivine-rich rocks generated at the mantle-crust transition, supporting their origin by melt-dunite reaction processes.

Acknowledgments

Andrea Risplendente is thanked for the valuable technical assistance during the work at the electron microprobe. Constructive reviews by Yan Liang and Alessio Sanfilippo improved the quality of this manuscript. This project has been supported by the People Programme (Marie Curie Actions) of the European Union's Seventh Framework Programme FP7/2007–2013/under REA-Grant Agreement No. 608001, 'ABYSS'. Funding was also provided by the Italian Ministry of Education, University and Research (MIUR) [PRIN-2015C5LN35] "Melt rock reaction and melt migration in the MORB mantle through combined natural and experimental studies".

References

Arai, S., Matsukage, K., 1996. Petrology of gabbro-troctolite-peridotite complex from Hess Deep, equatorial pacific: implications for mantle-melt interaction within the oceanic lithosphere. Proc. Ocean Drill. Program Sci. Results 147:135–155.

Arai, S., Matsukage, K., Isobe, E., Vysotskiy, S., 1997. Concentration of incompatible elements in oceanic mantle: effect of melt/wall interaction in stagnant or failed melt conduits within peridotite. Geochim. Cosmochim. Acta 61, 671–675.

Barnes, S.J., 1986. The effect of trapped liquid crystallization on cumulus mineral compositions in layered intrusions. Contrib. Mineral. Petrol. 93:524–531.

Basch, V., 2018. Melt-rock interactions in the oceanic lithosphere: microstructural and petro-geochemical constraints from ophiolites. PhD Thesis, University of Genova, 336 pp.

Basch, V., Rampone, E., Crispini, L., Ferrando, C., Ildefonse, B., Godard, M., 2018. From mantle peridotites to hybrid troctolites: textural and chemical evolution during melt-rock interaction history (Mt. Maggiore, Corsica, France). Lithos (this volume, in press)

Beck, A.R., Morgan, Z.T., Liang, Y., Hess, P.C., 2006. Dunite channels as viable pathways for mare basalt transport in the deep lunar mantle. Geophys. Res. Lett. 33:L01202.

Bédard, J.H., 1993. Oceanic crust as a reactive filter: synkinematic intrusion, hybridization, and assimilation in an ophiolitic magma chamber, western Newfoundland. Geology 21:77–80.

Bedard, J.H., 1994. A procedure for calculating the equilibrium distribution of trace elements among the minerals of cumulate rocks, and the concentration of trace elements in coexisting liquids. Chem. Geol. 118:143–153.

Bédard, J.H., Hebert, R., Berclaz, A., Varfalvy, V., 2000. Syntexis and the genesis of lower

oceanic crust. In: Dilek, Y., Moores, E.M., Elthon, D., Nicolas, A. (Eds.), Ophiolites and Oceanic Crust: New Insights From Field Studies and the Ocean Drilling Program, Special Paper. vol. 349. Geological Society of America, pp. 105–119.

Bender, J.F., Hodges, F.N., Bence, A.E., 1978. Petrogenesis of basalts from the project FAMOUS area: experimental study from 0 to 15 kbars. Earth and Planetary Science Letters 41:277–302.

Borghini, G., Rampone, E., Crispini, L., De Ferrari, R., Godard, M., 2007. Origin and emplace- ment of ultramafic-mafic intrusions in the Erro-Tobbio mantle peridotite (Ligurian Alps, Italy). Lithos 94:210–229.

Borghini, G., Rampone, E., 2007. Postcumulus processes in oceanic-type olivine-rich cumulates: the role of trapped melt crystallization versus melt/rock interaction. Contrib. Mineral. Petrol. 154:619–633.

Borghini, G., Fumagalli, P., Rampone, E., 2010. The Stability of Plagioclase in the Upper Mantle: Subsolidus Experiments on Fertile and Depleted Lherzolite. J. Petrol. 51:229-254.

Borghini, G., Fumagalli, P., Rampone, E., 2011. The geobarometric significance of plagioclase in mantle peridotites: a link between nature and experiments. Lithos 126:42–53.

Boudier, F., Nicolas, A., 1995. Nature of the Moho transition zone in the Oman Ophiolite. J. Petrol. 36:777–796.

Cawthorn, R.G. 1996. Models for incompatible trace element abundances in cumulus minerals and their application to plagioclase and pyroxenes in the Bushveld Complex. Contrib. Mineral. Petrol. 123:109–115.

Charlier, B., Auwera, J.V., Duchesne, J.C., 2005. Geochemistry of cumulates from the Bjerkreim-Sokndal layered intrusion (S. Norway) Part II. REE and the trapped liquid

fraction. Lithos 83:255–276.

Collier, M.L., Kelemen, P.B., 2010. The case for reactive crystallization at mid-ocean ridges. J. Petrol. 51:1913–1940

Coogan, L.A., Kempton, P.D., Saunders, A.D., Norry, M.J.,2000°. Melt aggregation within the crust beneath the Mid-Atlantic Ridge: evidence from plagioclase and clinopyroxene major and trace element compositions. Earth Planet. Sci. Lett. 176:245–257.

Coogan, L.A., Saunders, A.D., Kempton, P.D., Norry, M.J., 2000b. Evidence from oceanic gabbros for porous melt migration within a crystal mush beneath the Mid-Atlantic Ridge. Geochem. Geophys. Geosys. 1 paper number 2000GC000072.

Daines, M., Kohlstedt, D., 1994. The transition from porous to channelized flow due to melt/rock reaction during melt migration. Geophysical Reshearch Letters 21:145-148.

DePaolo, D.J., 1981. Trace element and isotopic effects of combined wallrock assimilation and fractional crystallization. Earth Planet. Sci. Lett. 53:189–202.

Dick, H.J.B., 1977. Evidence of partial melting in the Josephine Peridotite. In: H.J.B. Dick (Ed.), Magma Genesis. Portland, OR: Oregon Dept. Geol. Mineral Industries, 59-62.

Dick, H.J.B., Natland, J.H., Alt, J.C., et al., 2000. A long in-situ section of the lower ocean crust: results of ODP Leg 176 drilling at the Southwest Indian Ridge. Earth Planet. Sci. Lett. 179:31–51.

Dick, H.J.B., Tivey, M.A., Tucholke, B.E., 2008. Plutonic founda- tion of a slow-spread ridge segment: the oceanic core complex at Kane Megamullion, 23830'N, 45820'W. Geochemistry, Geophysics, Geosystems 9, Q05014.

Dick, H.J.B., Lissemberg, C.J., Warren, J.M., 2010. Mantle melting, melt transport, and delivery beneath a slow-spreading ridge: the paleo-MAR from 23815'N to 23845'N. Journal of Petrology 51:425–467.

Dijkstra, A.H., Barth, M.G., Drury, M.R., Mason, P.R.D., Vissers, R.L.M., 2003. Diffuse porous melt flow and melt-rock reaction in the mantle lithosphere at a slow-spreading ridge: a struc- tural petrology and LA-ICP-MS study of the Othris Peridotite Massif (Greece). Geochem. Geophys. Geosyst. 4:8613.

Drouin, M., Godard, M., Ildefonse, B., Bruguier, O., Garrido, C.J., 2009. Geochemical and petrographic evidence for magmatic impregnation in the oceanic lithosphere at Atlantis Massif, Mid-Atlantic Ridge (IODP Hole U1309D, 30°N). Chem. Geol. 264: 71–88.

Drouin, M., Ildefonse, B., Godard, M., 2010. A microstructural imprint of melt impregna- tion in slow spreading lithosphere: olivine-rich troctolites from the Atlantis Massif, Mid-Atlantic Ridge, 30°N, IODP Hole U1309D. Geochem. Geophys. Geosyst. 11:1–21.

Dygert, N., Liang, Y., Kelemen, P.B., 2016. Formation of plagioclase lherzolite and associated Dunite-Harzburgite-Lherzolite sequences by multiple episodes of melt percolation and melt-rock reaction: an example from the Trinity ophiolite, California, USA. Journal of Petrology 57:815–838.

Ferrando, C., Godard, M., Ildefonse, B., Rampone, E., 2018. Melt transport and mantle assimi- lation at Atlantis Massif (IODP site U1309): evidence from chemical profiles along olivine crystallographic axes. Lithos (this volume, in press).

Fumagalli, P., Borghini, G., Rampone, E., Poli, S., 2017. Experimental calibration of Forsterite–Anorthite–Ca-Tschermak–Enstatite (FACE) geobarometer for mantle peridotites. Contrib. Mineral. Petrol. 172:38.

Gillis, K., et al. (2014) Primitive layered gabbros from fast-spreading lower oceanic crust: Nature, 505:204–207.

Godard, M., Awaji, S., Hansen, H.E., Hellebrand, E., Brunelli, D., Johnson, K.T.M.,

Yamasaki, T., Maeda, J., Abratis, M., Christie, D., Kato, Y., Mariet, C., Rosner, M., 2009. Geochemistry of a long in-situ section of intrusive slow-spread lithosphere: Results from IODP Site U1309 (Atlantis Massif, 30°N Mid-Atlantic-Ridge). Earth and Planetary Science Letters 279:110–122.

Grove, T.L., Kinzler, R.J., Bryan, W.B., 1992. Fractionation of mid-ocean ridge basalt (MORB). In: Phipps Morgan, J., Blackman, D. K. & Sinton, J. M. (eds) Mantle Flow and Melt Generation at Mid-ocean Ridges. Geophysical Monograph, American Geophysical Union 71:281–310.

Hart, S.R., Davis, K.E., 1978. Nickel partitioning between olivine and silicate melt. Earth Planet. Sci. Lett. 40:203–219.

Higgie, K., Tommasi, A., 2012. Feedbacks between deformation and melt distribution in the crust–mantle transition zone of the Oman ophiolite. Earth Planet. Sci. Lett. 359–360:61–72.

Holness, M.B., Anderson, A.T., Martin, V.M., Maclennan, J., Passmore, E., Schwindinger, K., 2007. Textures in partially solidified crystalline nodules: a window into the pore structure of slowly cooled mafic intrusions. J. Petrol. 48:1243–1264. https://doi.org/10.1093/petrology/egm016

Husen, A., Almeev, R., Holtz, F., 2016. The Effect of H_2O and Pressure on Multiple Saturation and Liquid Lines of Descent in Basalt from the Shatsky Rise. Journal of Petrology 57:309–344.

Kelemen, P.B., Joyce, D.B., Webster, J.D., Holloway, J.R., 1990. Reaction between ultramafic rock and fractionating basaltic magma. II. Experimental investigations of reaction between olivine tholeiite and harzburgite at 1150-1050 °C and 5 kbar. J. Petrol. 31: 99–134.

Kelemen, P.B., Shimizu, N., Salters, V.J.M., 1995a. Extraction of mid-ocean-ridge basalt

from the upwelling mantle by focused flow of melt in dunite channels. Nature 375:747–753.

Kelemen, P.B., Whitehead, J.A., Aharonov, E., Jordahl, K.A., 1995b. Experiments on flow fo- cusing in soluble porous media, with applications to melt extraction from the mantle. Journal of Geophysical Research 100:475–496.

Kelemen, P.B., Kikawa, E., Miller, D.J., Shipboard Scientific Party, 2007. 1. Leg 209 summary: processes in a 20-km-thick conductive boundary layer beneath the Mid-Atlantic Ridge, 14°–16°N. Proceedings of the Ocean Drilling Program, Scientific Results vol. 209. Ocean Drilling Program, College Station TX: pp. 1–33.

Koepke, J., Schoenborn, S., Oelze, M., Wittmann, H., Feig, S.T., Hellebrand, E., Boudier, F., Schoenberg, R., 2009. Petrogenesis of crustal wehrlites in the Oman ophiolite: experiments and natural rocks. Geochem. Geophys. Geosyst. 10:Q10002.

Kvassnes, A.J.S., Grove, T.L., 2008. How partial melts of mafic lower crust affect ascending magmas at oceanic ridges. Contrib. Mineral. Petrol. 156:49–71.

Lambart, S., Laporte, D., Schiano, P., 2009. An experimental study of focused magma transport and basalt-peridotite interactions beneath mid-ocean ridges: implications for the generation of primitive MORB compositions. Contrib. Mineral. Petrol. 157:429–451.

Lissenberg, C.J., Dick, H.J.B., 2008. Melt-rock reaction in the lower oceanic crust and its implications for the genesis of mid-ocean ridge basalt. Earth Planet. Sci. Lett. 271:311–325.

Lissenberg, C.J., MacLeod, C.J., Howard, K.A., Godard, M., 2013. Pervasive reactive melt migra- tion through fast-spreading lower oceanic crust (Hess Deep, equatorial Pacific Ocean). Earth Planet. Sci. Lett. 361:436–447.

Longhi, J., Fram, M., Vander Auwera, J., Montieth, J., 1993. Pressure effects, kinetics, and

rheology of anorthositic and related magmas. American Mineralogist, 78:1016–1030.

Matzen, A.K., Baker, M.B., Beckett, J.R., Stolper, E.M., 2013. The temperature and pressure dependence of nickel partitioning between olivine and silicate melt. J. Petrol. 54:2521–2545.

Matzen, A., Baker, M., Beckett, J., Wood, B., Stolper, E., 2017. The effect of liquid composition on the partitioning of Ni between olivine and silicate melt. Contrib. Mineral. Petrol. 172:3.

Meyer, P.S., Dick, H.J.B., Thomson, G., 1989. Cumulates gabbro from the Southwest Indian Ridge, 54° S–7°13' E: implication for magmatic processes at a slow spreading ridge. Contrib. Mineral. Petrol. 103:44–63.

Morgan, Z., Liang, Y., 2003. An experimental and numerical study of the kinetics of harzburgite reactive dissolution with applications to dunite dike formation. Earth and Planetary Science Letters 214:59-74

Morgan, Z., Liang, Y., 2005. An experimental study of the kinetics of lherzolite reactive dissolution with applications to melt channel formation. Contributions to Mineralogy and Petrology 150:369-385.

Morgan, Z., Liang, Y., Kelemen, P., 2005. Significance of the concentration gradients associated with dunite bodies in the Josephine and Trinity ophiolites. Geochemistry, Geophysics, Geosystem 9, Q07025.

Namur, O., Charlier, B., Toplis, M.J., Vaunder Auwera, J., 2012. Prediction of plagioclase-melt equilibria in anhydrous silicate melts at 1-atm. Contrib. Mineral. Petrol. 163:133–150.

O'Driscoll, B., Donaldson, C.H., Troll, V.R., Jerram, D.A., Emeleus, C.H., 2007. An origin for harrisitic and granular olivine in the Rum layered suite, NW Scotland: a crystal size distribution study. J. Petrol. 48:253–270.

Panjasawatwong, Y., Danyushevsky, L.V., Crawford, A.J., Harris, K.L., 1995. An experimental study of the effects of melt composition on plagioclase-melt equilibria at 5 and 10 kbar: implications for the origin of magmatic high-An plagioclase. Contrib. Mineral. Petrol. 118: 420.

Paquet, M., Cannat, M., Brunelli, D., Hamelin, C., Humler, E., 2016. Effect of melt/mantle interactions on MORB chemistry at the easternmost Southwest Indian Ridge (61°-67°E). Geochem. Geophys. Geosyst. 17.

Pec, M., Holtzman, B.K., Zimmerman, M., Kohlstedt, D., 2015. Reaction infiltration instabilities in experiments on partially molten mantle rocks. Geology 43:575–578.

Pirard, C., Hermann, J., O'Neill, H.S.T.C., 2013. Petrology and geochemistry of the crust-mantle boundary in a nascent arc, Massif du Sud ophiolite, New Caledonia, SW Pacific. Journal of Petrology 54:1759–1792.

Quick, J.E., 1981. The origin and significance of large, tabular dunite bodies in the Trinity Peridotite, Northern California. Contrib. Mineral. Petrol. 78: 413–422.

Rampone, E., Borghini, G., 2008. Melt migration and intrusion in the Erro-Tobbio peridotites (Ligurian Alps, Italy): Insights on magmatic processes in extending lithospheric mantle. Eur. J. Min. 20:573–585.

Rampone, E., Romairone, A., Hofmann, A.W., 2004. Contrasting bulk and mineral chemistry in depleted peridotites: evidence for reactive porous flow. Earth Planet. Sci. Lett. 218:491–506.

Rampone, E., Piccardo, G.B., Hofmann, A.W., 2008. Multi-stage melt–rock interaction in the Mt. Maggiore (Corsica, France) ophiolitic peridotites: microstructural and geochemical evidence. Contrib. Mineral. Petrol. 156:453.

Rampone, E., Borghini, G., Godard, M., Ildefonse, B., Crispini, L., Fumagalli, P., 2016. Melt/rock reaction at oceanic peridotite/gabbro transition as revealed by trace element

chemistry of olivine. Geochim. Cosmochim. Acta 190:309–331.

Renna, M.R., Tribuzio, R., 2011. Olivine-rich troctolites from Ligurian ophiolites (Italy): evidence for impregnation of replacive mantle conduits by MORB-type melts. Journal of Petrology 52:1763–1790.

Renna, M.R., Tribuzio, R., Ottolini, L., 2016. New perspectives on the origin of olivine-rich troctolites and associated harrisites from the Ligurian ophiolites (Italy). J. Geol. Soc. Lond. 173:916–932.

Ross, D.K., Elthon, D., 1997. Cumulus and postcumulus crystallization in the oceanic crust: major- and trace-element geochemistry of Leg 153 gabbroic rocks. Proc. Ocean Drill. Program Sci. Results 153:333–353.

Sanfilippo, A., Tribuzio, R., 2011. Melt transport and deformation history in a nonvolcanic ophiolitic section, northern Apennines, Italy: Implications for crustal accretion at slow spreading settings. Geochemistry, Geophysics, Geosystems 12:1–34.

Sanfilippo, A., Tribuzio, R., 2013. Building of the deepest crust at a fossil slow-spreading centre (Pineto gabbroic sequence, Alpine Jurassic ophiolites). Contrib. Mineral. Petrol. 165:705–721.

Sanfilippo, A., Tribuzio, R., Tiepolo, M., 2014. Mantle-crust interactions in the oceanic lithosphere: constraints from minor and trace elements in olivine. Geochim. Cosmochim. Acta 141:423–439.

Sanfilippo, A., Morishita, T., Kumagai, H., Nakamura, K., Okino, K., Hara, K., Tamura, A., Arai, S., 2015. Hybrid troctolites from mid-ocean ridges: inherited mantle in the lower crust. Lithos 232:124–130.

Sanfilippo, A., Dick, H.J.B., Ohara, Y., Tiepolo, M., 2016. New insights on the origin of troctolites from the breakaway area of the Godzilla Megamullion (Parece Vela back-arc basin): the role of melt-mantle interaction on the composition of the lower crust.

Island Arc 25:220–234.

Saper, L., Liang, Y., 2014. Formation of plagioclase-bearing peridotite and plagioclase-bearing wehrlite and gabbro suite through reactive crystallization: an experimental study. Contrib. Mineral. Petrol. 167:1–16.

Soustelle, V., Walte, N.P., Geeth, M.A., Manthilake, M., Frost, D.J., 2014. Melt migration and melt-rock reactions in the deforming Earth's upper mantle: experiments at high pressure and temperature. Geology 42:83–86.

Stolper, E., 1980. A phase diagram for mid-ocean ridge basalts: Preliminary results and implications for petrogenesis. Contributions to Mineralogy and Petrology 74:13–27.

Suhr, G., Hellebrand, E., Johnson, K., Brunelli, D., 2008. Stacked gabbro units and intervening mantle: a detailed look at a section of IODP leg 305, hole U1309D. Geochem. Geophys. Geosyst. 9.

Takagi, D., Sato, H., Nakagawa, M., 2005. Experimental study of a low-alkali tholeiite at 1–5 kbar: optimal condition for the crystallization of high-An plagioclase in hydrous arc tholeiite. Contrib. Mineral. Petrol. 149:527.

Tursack, E., Liang, Y., 2012. A comparative study of melt-rock reactions in the mantle: laboratory dissolution experiments and geological field observations. Contributions to Mineralogy and Petrology 163:861–876.

Ulmer, P, Luth, R., 1991. The graphite–COH fluid equilibrium in P, T, fO_2 space. Contributions to Mineralogy and Petrology 106:265–272.

Van Den Bleeken, G., Müntener, O., Ulmer, P., 2010. Reaction Processes between Tholeiitic Melt and Residual Peridotite in the Uppermost Mantle: an Experimental Study at 0·8 GPa. Journal of Petrology 51:153–183.

Van den Bleeken, G., Müntener, O., Ulmer, P., 2011. Melt variability in percolated peridotite: an experimental study applied to reactive migration of tholeiitic basalt in the upper

mantle. Contrib. Mineral. Petrol. 161:921–945.

Villiger, S., Ulmer, P., Muntener, O., Thompson, A.B., 2004. The liquid line of descent of anhydrous, mantle-derived, tholeiitic liquids by fractional and equilibrium crystallizationc□an experimental study at 1.0 GPa. Journal of Petrology 45:2369–2388.

Villiger, S., Muentener, O., Ulmer, P., 2007. Crystallization pressures of mid-ocean ridge basalts derived from major element variations of glasses from equilibrium and fractional crystallization experiments. Journal of Geophysical Research: Solid Earth 112:159–184.

Wang, C., Liang, Y., Xu, W., Dygert, N., 2013. Effect of melt composition on basalt and peridotite interaction: laboratory dissolution experiments with applications to mineral compositional variations in mantle xenoliths from the North China Craton. Contrib. Mineral. Petrol. 166:1469–1488.

Figure Captions

Figure 1: (a) Three-layer experimental setup of the graphite lined platinum capsule used in this study. (b) Temperature vs. time path of the dissolution-crystallization experiments.

Figure 2: (a) Starting synthetic basalts (AH3, AH6 and HDRBC) plotted in the diagrams (a) X_{Mg} = Mg/(Mg+Fe) vs. X_{Ca} = Ca/(Ca+Na) and (b) TAS (Total Alkali versus Silica). AH3 and AH6 compositions are from Husen et al. (2016); HDRBC is the bulk composition of the Hess Deep Rise Basaltic Crust from Gillis et al. (2014). Grey circles are the compositions of Atlantic and Pacific MORBs (PetDB, http://www.earthchem.org/petdb).

Figure 3: Representative Back-Scattered-Electron (BSE) images showing textures in reactive experiments; a) Panoramic view of the capsule of the isothermal run OM15 (0.7 GPa, 1250°C, 24 hrs. AH6 starting melt), showing glass layer at the bottom, glass-bearing olivine-rich layer in the middle, and glas trapped within the carbon spheres at the top of the capsule; b) Subhedral crystals of olivine with embayed, lobate and cusped boundaries against the glass in OM15 (0.7 GPa, 1250°C, AH6 starting melt); c) Panoramic view of the capsule of step-cooled experiment OM02 (0.5 GPa, step-cooled down to 1150°C, AH6 starting melt) consisting of glass-bearing olivine-gabbro overlain by olivine-rich layer with olivine, plagioclase, clinopyroxene; d) Interstitial plagioclase and clinopyroxene within olivine matrix in olivine-rich layer of run OM03 (0.5 GPa, step-cooled down to 1150°C, HDRBC starting melt); e) Poikilitic plagioclase including rounded olivines and partially resorbed subhedral olivines in the olivine-rich layer of run OM02 (0.5 GPa, step-cooled down to 1150°C, AH6 starting melt); f) Sharp and straight boundaries between interstitial plagioclase and clinopyroxene suggesting co-precipitation; small rounded olivines included into poikilitic plagioclase in run OM20 (0.7 GPa, step-cooled down to 1150°C, AH6 starting melt); g) co-precipitation of interstitial plagioclase and clinopyroxene in olivine-rich layer of run OM02 (0.5 GPa, step-cooled down to 1150°C, AH6 starting melt); h) interstitial glass in olivine-rich layer of run OM02 (0.5 GPa, step-cooled down to 1150°C, AH6 starting melt).

Figure 4: X_{Mg} [X_{Mg} = Mg/(Mg+Fe)] and NiO content (wt.%) in olivines as a function of distance (in µm) from the interface with gabbro layer (or glass layer for the isothermal experiment OM15). Distance = 0 µm marks the boundary between gabbro and olivine-rich layer boundary; a) and b) results in experiments at 0.5 GPa; c) and d) results in experiments at 0.7 GPa. Full and empty symbols represent cores and rims, respectively. Grey vertical band is the composition of starting San Carlos olivine.

Figure 5. Anorthite content [X_{an} = Ca/(Ca+Na] in plagioclase as a function of distance along the olivine-rich layer in experiments at 0.5 (a) and 0.7 (b) GPa. Distance = 0 μm marks the boundary between gabbro and olivine-rich layer boundary. Also reported are the compositions of plagioclase from equilibrium crystallization experiments by Husen et al. (2016) on AH6 melt at 0.4 GPa, 1150 and 1200°C (a), and at 0.7 GPa on AH6 and AH3 melts, 1150, 1200 and 1225°C (b).

Figure 6: X_{Mg} [X_{Mg} = Mg/(Mg+Fe_{tot})] and TiO_2 content (wt.%) in clinopyroxene as a function of distance along the olivine-rich layer in experiments at 0.5 GPa (a, b) and 0.7 GPa (c, d). Distance = 0 μm marks the boundary between gabbro and olivine-rich layer boundary. Also reported are the compositions of clinopyroxene from equilibrium crystallization experiments by Husen et al. (2016) on AH6 melt at 0.4 GPa, 1150, 1175 and 1200°C (a, b), and on AH6 and AH3 melts at 0.7 GPa, 1150, 1200 and 1225°C (c, d).

Figure 7: X_{Mg} [X_{Mg} = Mg/(Mg+Fe_{tot})] vs. Cr_2O_3 (a), Al_2O_3 (b), Na_2O (c), and TiO_2 (d) contents (wt.%) in clinopyroxene from reaction experiments at 0.5 and 0.7 GPa, compared to data from natural troctolites: Atlantis Massif, Mid Atlantic Ridge 30°N (Suhr et al., 2008; Drouin et al., 2009; Ferrando et al., 2018); Godzilla Megamullion, Philippine Sea (Sanfilippo et al., 2013); Kane Megamullion, Mid Atlantic Ridge (Lissenberg and Dick, 2008); Erro-Tobbio ophiolites, Western Alps (Borghini et al., 2007; Borghini and Rampone, 2007; Rampone et al., 2016); Internal Ligurides ophiolites, Northern Apennines (Renna and Tribuzio, 2011); Pineto ophiolites, Corsica (Sanfilippo and Tribuzio, 2013).

Figure 8: Phase maps derived by combining X-ray concentration maps (Ca, Mg, Al) on

olivine-rich layers in step cooled experiments OM20 (a) and OM02 (b), performed with the starting melt AH6, at 0.5 and 0.7 GPa, respectively. Olivine in red, clinopyroxene in blue, plagioclase in green, glass in white. (c) Phase abundances in olivine-rich layers of step-cooled experiments.

Figure 9: X_{Mg} vs. NiO content in olivine in reaction experiments at 0.5 and 0.7 GPa compared with data from natural troctolites. Symbols and references are as in Figure 7. Data of Erro-Tobbio troctolites include additional olivine compositions from Basch (2018). Yellow star represents the composition of starting San Carlos olivine.

Figure 10: X_{Mg} in olivine vs. and X_{an} in plagioclase in reaction experiments at 0.5 and 0.7 GPa compared with data from natural troctolites. Symbols and references are as in Figure 7 and 9. Red dashed line is the equilibrium crystallization path obtained by linear regression of data from experiments on AH6 melt by Husen et al. (2016). Black and open circles represent models of reactive crystallization computed starting from a residual mantle harzburgite and a primitive MORB-type melt at 0.6 GPa assuming respectively 1 and 3 grams of mantle assimilation per 1°C of cooling (Sanfilippo et al., 2016).

Table 1 Compositions of starting materials.

	San Carlos Olivine (n=18)[c]	HDRBC[a]	AH6[b]	AH3[b]
SiO_2	40.68(32)	48.25	47.70	49.25
TiO_2	0.00(0)	0.83	0.89	1.45
Al_2O_3	0.01(1)	16.57	16.76	15.64
Cr_2O_3	0.03(3)		0.09	0.00
FeO	8.90(26)	7.68	9.51	10.47
MnO	0.12(4)	0.14	0.19	0.17
NiO	0.37(4)		0.00	0.00
MgO	49.14(20)	12.37	8.62	7.99
CaO	0.07(2)	11.90	13.80	12.16
Na_2O	0.01(1)	1.80	2.28	2.49
K_2O	0.00(0)	0.11	0.10	0.18
P_2O_5			0.05	0.20
Total	99.34	99.65	99.94	99.80
X_{Mg}[d]	0.908(5)	0.742	0.618	0.580
X_{Ca}[e]		0.790	0.770	0.730

[a] from Gillis et al. (2014), [b] from Husen et al. (2016), [c] n: number of analysis. In the first column, in parentheses we report the standard deviation (1σ) given in terms of least unit; e.g. 47.68 (32) is 47.568 ± 0.32.
[d] X_{Mg}= Mg/(Mg+Fe), uncertainties of XMg have been obtained by error propagation.
[e] X_{Ca}= Ca/(Ca+Na).

Table 2 Run conditions and final phase assemblages.

	Temperature (°C)		Cooling Process	Starting Melt	Total run duration (h)	Lithology of the ol-rich layer
	Initial	Final				
Runs at 0.5 GPa						
OM02	1300	1150	Step	AH6	72	ol-rich troctolite
OM03	1300	1150	Step	HDRBC	72	ol-rich troctolite
Runs at 0.7 GPa						
OM15	1250	1250	None	AH6	24	ol, glass
OM20	1300	1150	Step	AH6	72	pl- and cpx-bearing dunite
OM21 (no melt trap)	1300	1150	Step	AH6	72	pl- and cpx-bearing dunite
OM22	1300	1150	Step	AH3	72	pl- and cpx-bearing dunite

ol= olivine; pl=plagioclase; cpx=clinopyroxene; gl=glass.

Step: step-cooled temperature path with a ramp of 10°C/minute.

Highlights

- The origin of olivine rich troctolites by melt-olivine reaction have been experimentally investigated
- melt-olivine reaction step-cooled experiments from 1300 down to 1150°C, at constant pressure (0.5 and 0.7 GPa)
- textural development in experiments is comparable with disequilibrium features in natural olivine-rich troctolites
- Modal abundance and mineral chemistry is controlled by starting melt composition and melt-olivine ratio
- Experimental data shed lights on the significance of melt-rock reactions in the formation of oceanic lithosphere

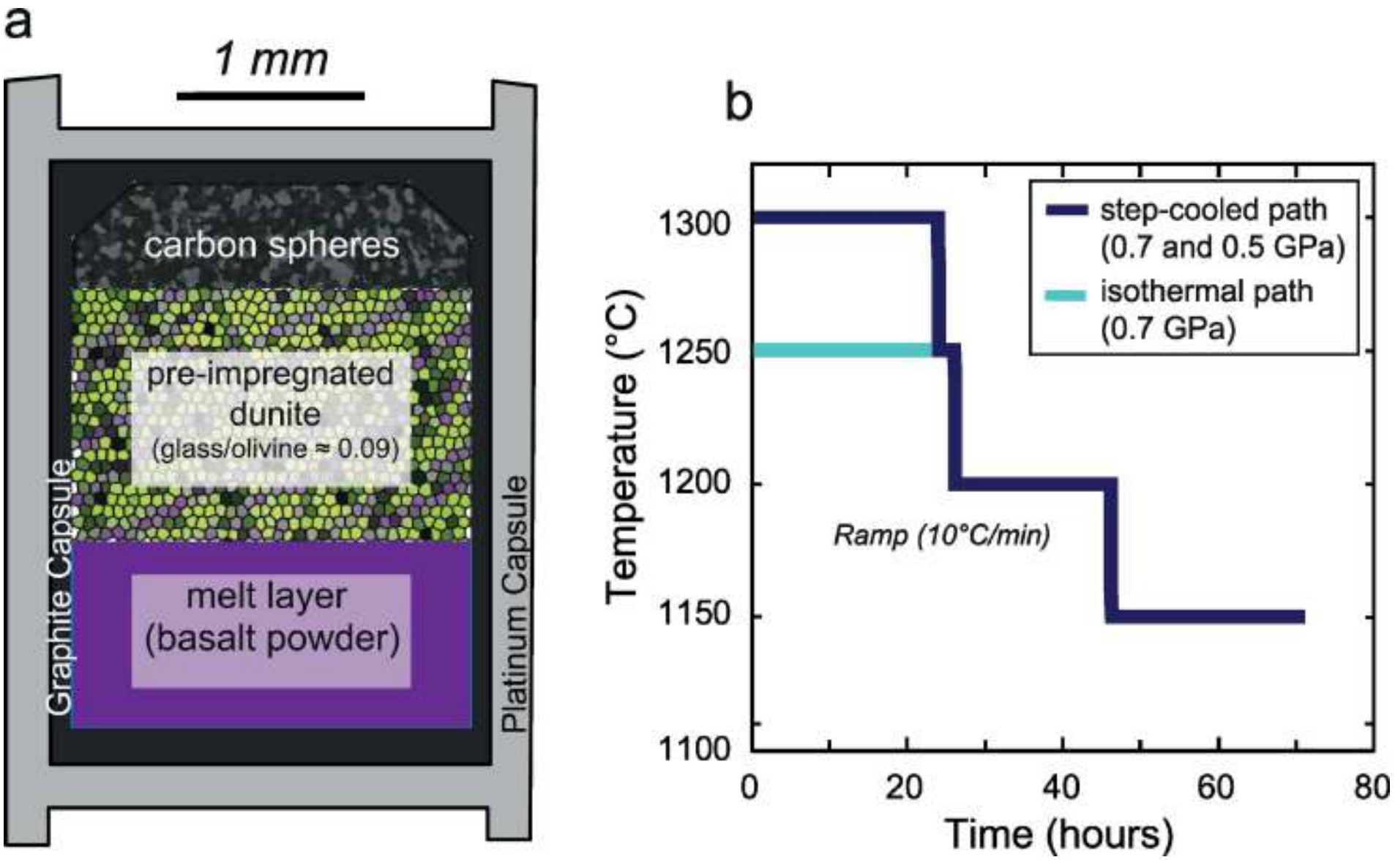
a
1 mm
carbon spheres
pre-impregnated
dunite
(glass/olivine ≈ 0.09)
melt layer
(basalt powder)
Graphite Capsule
Platinum Capsule
b
step-cooled path
(0.7 and 0.5 GPa)
isothermal path
(0.7 GPa)
Ramp (10°C/min)
Temperature (°C)
1300
1250
1200
1150
1100
0
20
40
60
80
Time (hours)

Figure 1

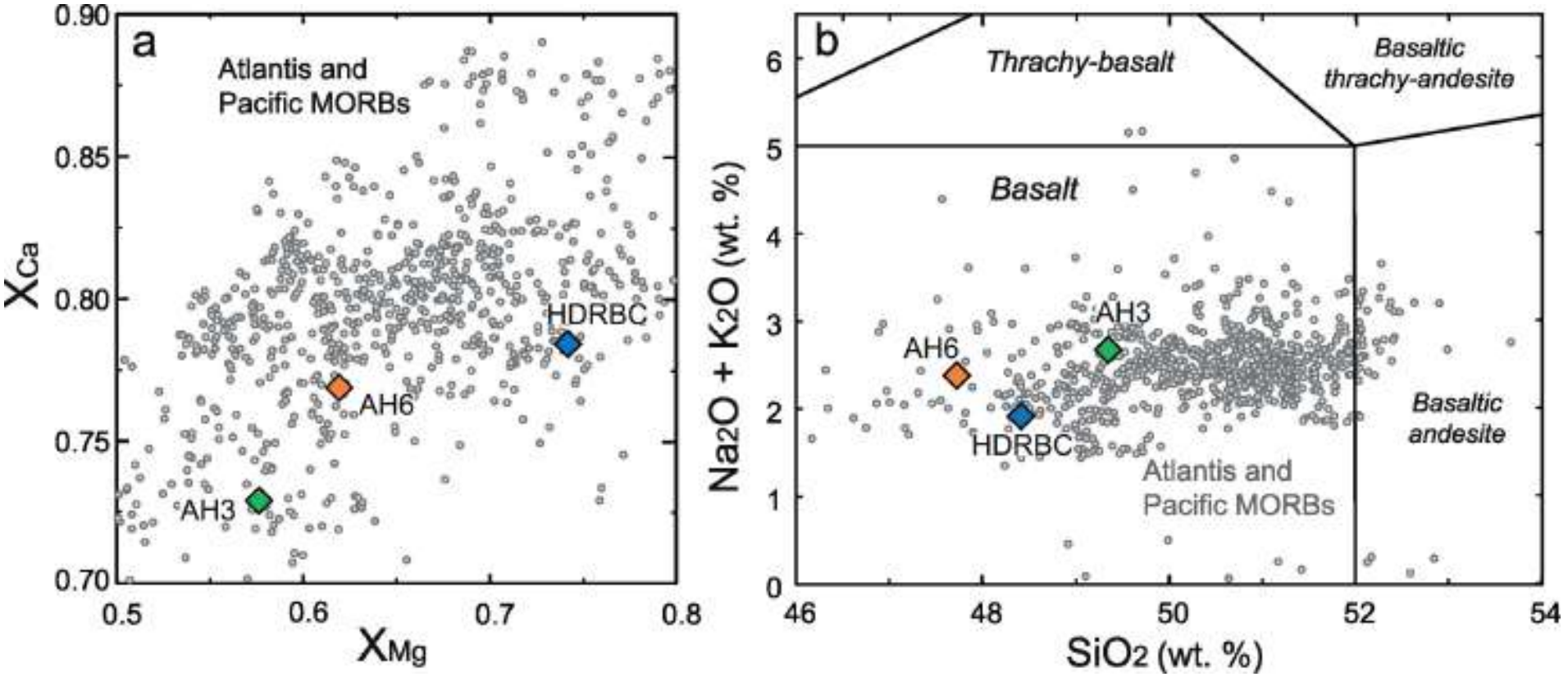
a
Atlantis and
Pacific MORBs
HDRBC
AH6
AH3
0.90
0.85
0.80
0.75
0.70
0.5
0.6
0.7
0.8
XCa
XMg
b
Thrachy-basalt
Basaltic
thrachy-andesite
Basalt
Basaltic
andesite
AH3
AH6
HDRBC
Atlantis and
Pacific MORBs
6
5
4
3
2
1
0
46
48
50
52
54
Na2O + K2O (wt. %)
SiO2 (wt. %)

Figure 2

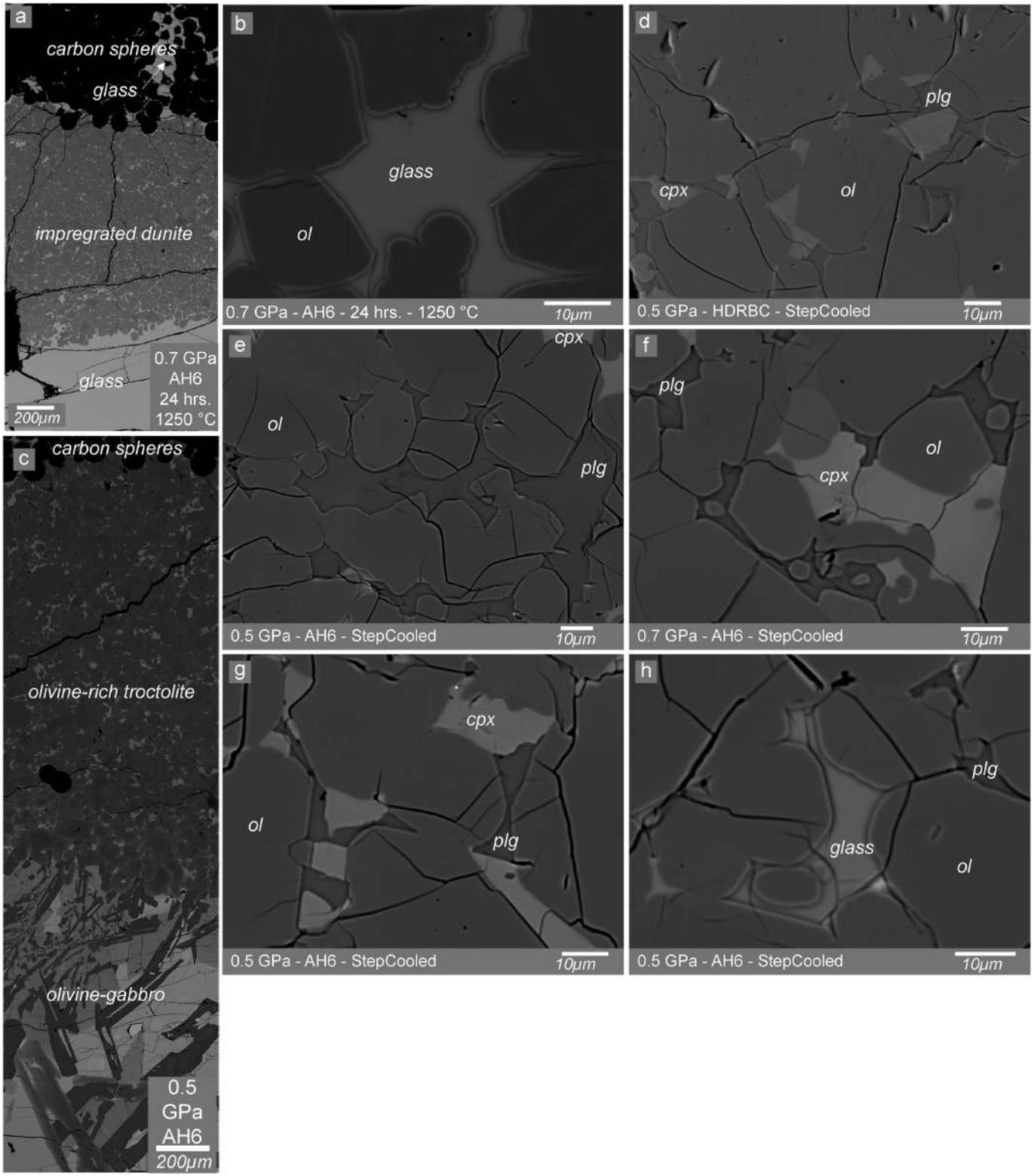
a
carbon spheres
glass
impregrated dunite
glass
0.7 GPa
AH6
24 hrs.
1250 °C
200µm
b
glass
ol
0.7 GPa - AH6 - 24 hrs. - 1250 °C
10µm
d
plg
cpx
ol
0.5 GPa - HDRBC - StepCooled
10µm
c
carbon spheres
olivine-rich troctolite
olivine-gabbro
0.5
GPa
AH6
200µm
e
cpx
ol
plg
0.5 GPa - AH6 - StepCooled
10µm
f
plg
ol
cpx
0.7 GPa - AH6 - StepCooled
10µm
g
cpx
ol
plg
0.5 GPa - AH6 - StepCooled
10µm
h
plg
glass
ol
0.5 GPa - AH6 - StepCooled
10µm

Figure 3

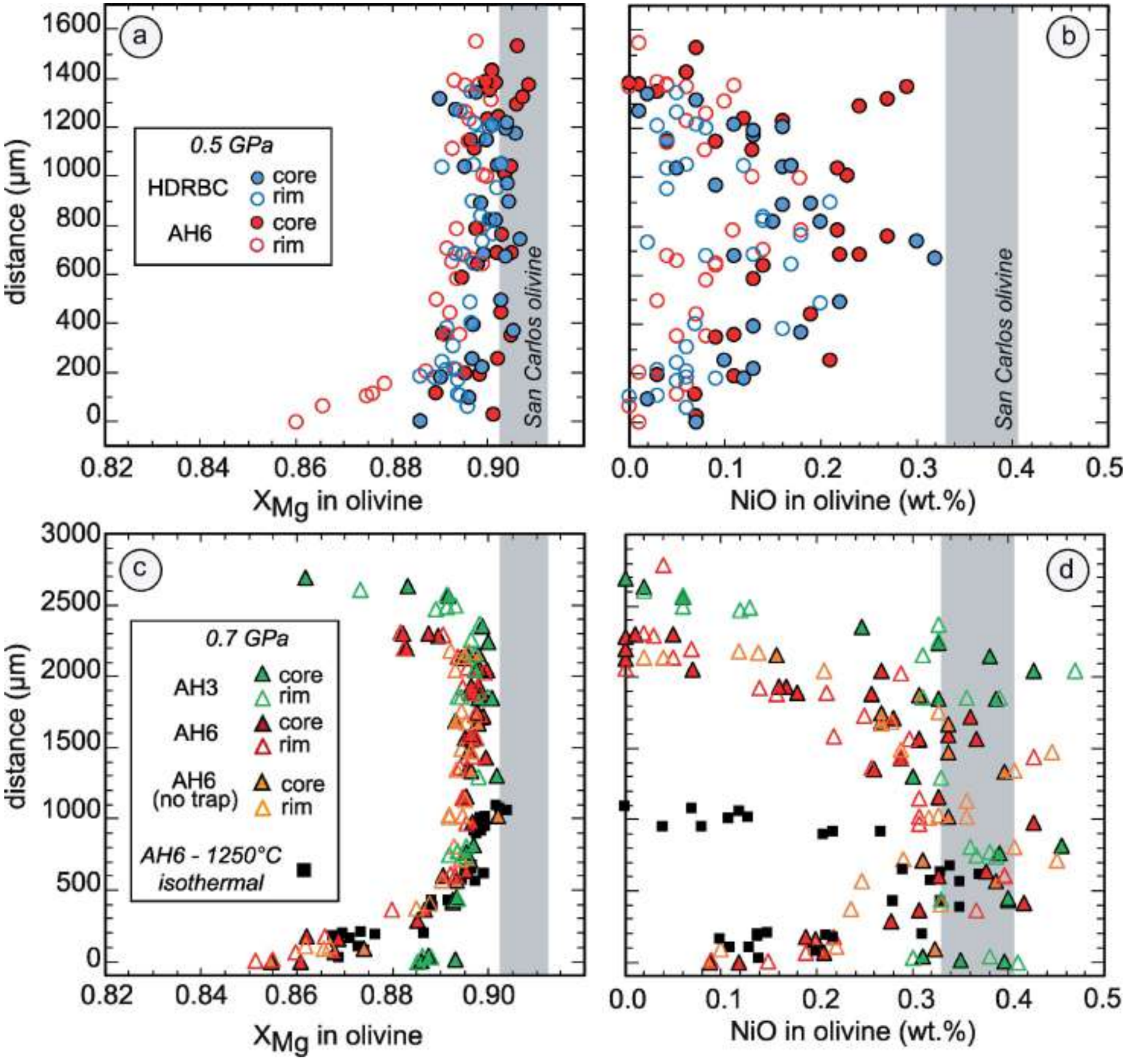
a
b
c
d
0.5 GPa
HDRBC
AH6
core
rim
core
rim
0.7 GPa
AH3
AH6
AH6 (no trap)
AH6 - 1250°C isothermal
San Carlos olivine
distance (µm)
X_Mg in olivine
NiO in olivine (wt.%)

Figure 4

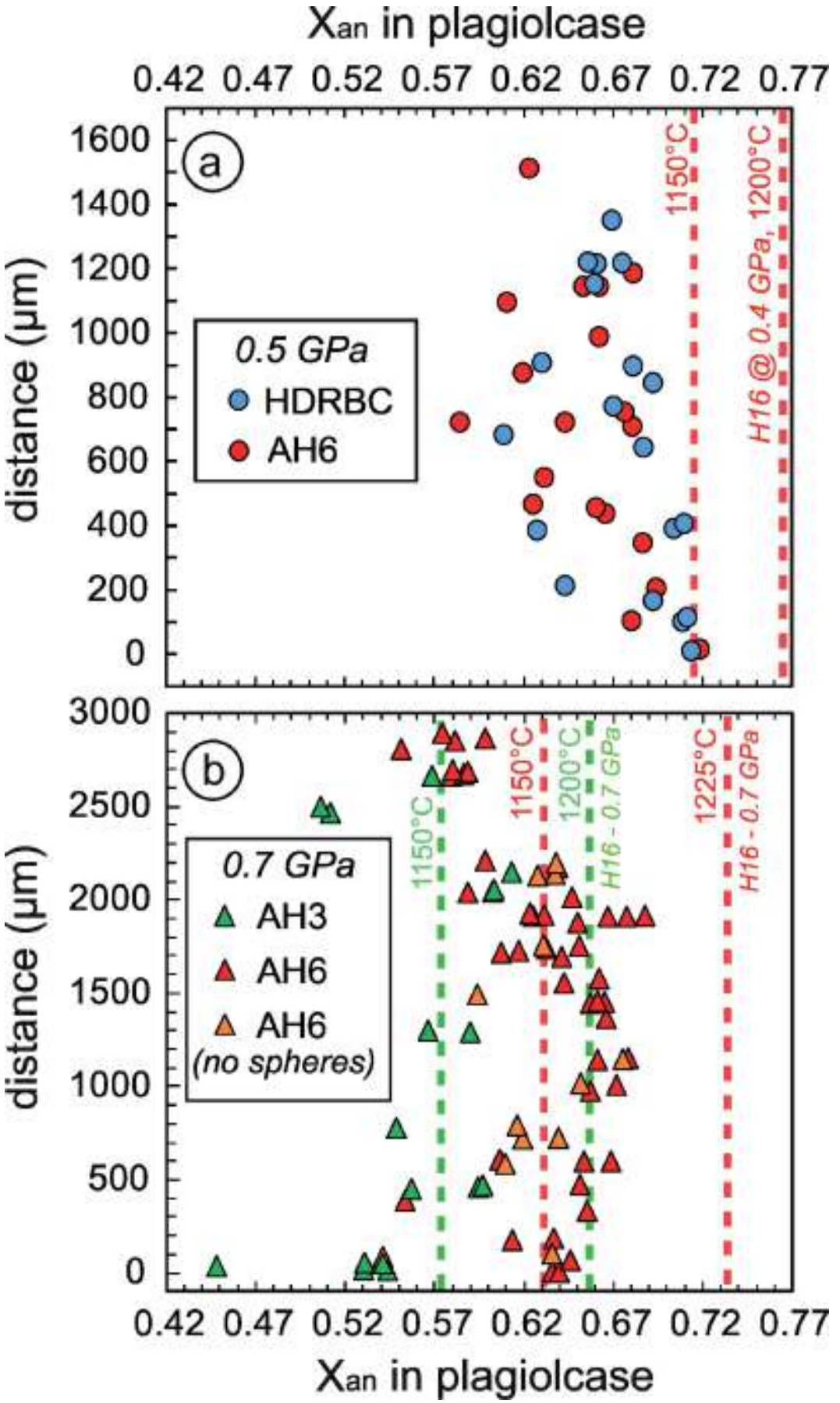
Xan in plagiolcase
0.42 0.47 0.52 0.57 0.62 0.67 0.72 0.77
a
distance (µm)
1600
1400
1200
1000
800
600
400
200
0
0.5 GPa
HDRBC
AH6
1150°C
H16 @ 0.4 GPa, 1200°C
b
3000
2500
2000
1500
1000
500
0
0.7 GPa
AH3
AH6
AH6
(no spheres)
1150°C
1150°C
1200°C
H16 - 0.7 GPa
1225°C
H16 - 0.7 GPa
0.42 0.47 0.52 0.57 0.62 0.67 0.72 0.77
Xan in plagiolcase

Figure 5

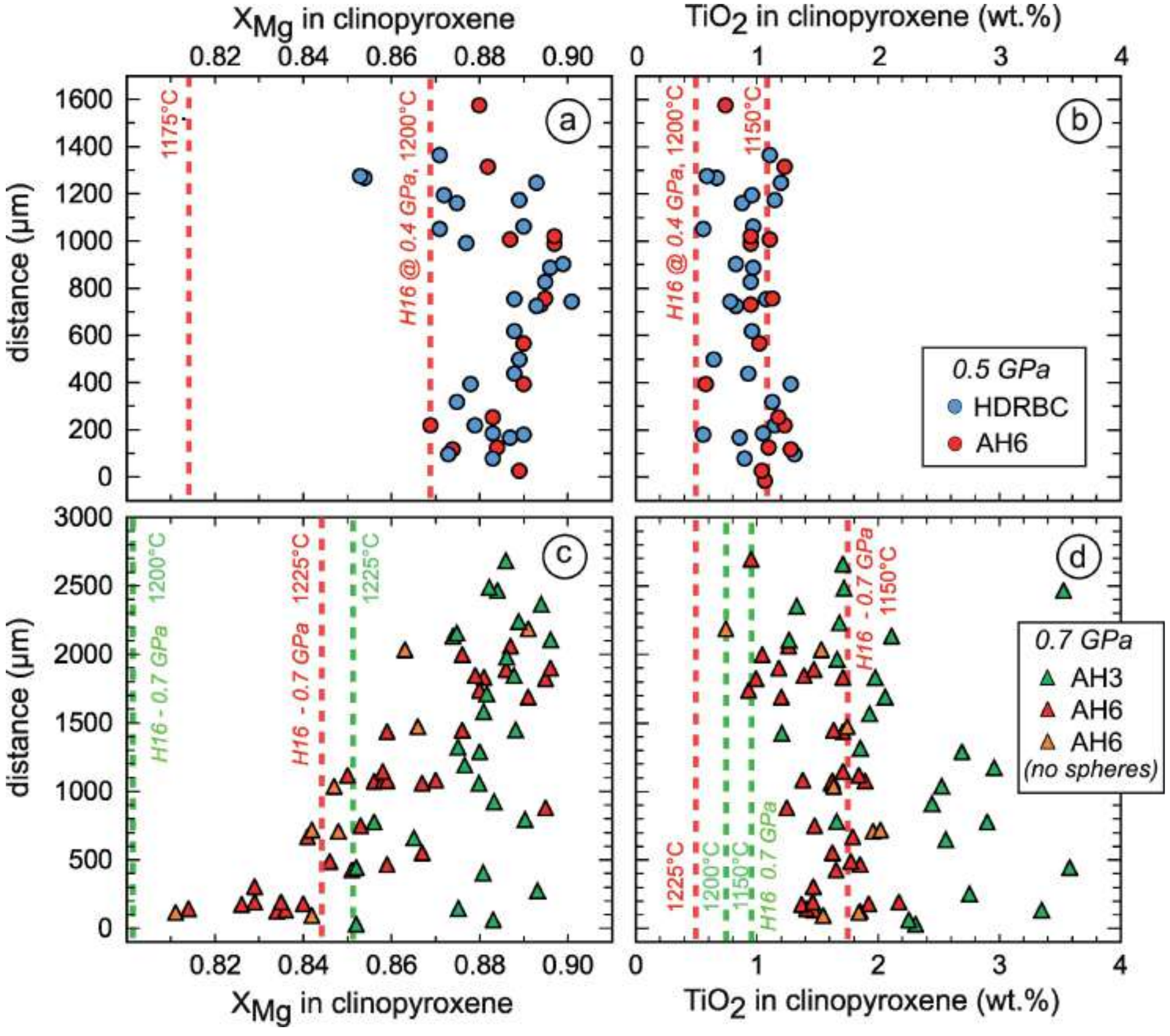
X_{Mg} in clinopyroxene
0.82
0.84
0.86
0.88
0.90
TiO_2 in clinopyroxene (wt.%)
0
1
2
3
4
distance (µm)
1600
1400
1200
1000
800
600
400
200
0
3000
2500
2000
1500
1000
500
a
b
c
d
1175°C
H16 @ 0.4 GPa, 1200°C
1150°C
H16 - 0.7 GPa 1200°C
H16 - 0.7 GPa 1225°C
1225°C
H16 - 0.7 GPa 1150°C
1225°C
1200°C
1150°C
H16 0.7 GPa
0.5 GPa
HDRBC
AH6
0.7 GPa
AH3
AH6
AH6
(no spheres)

Figure 6

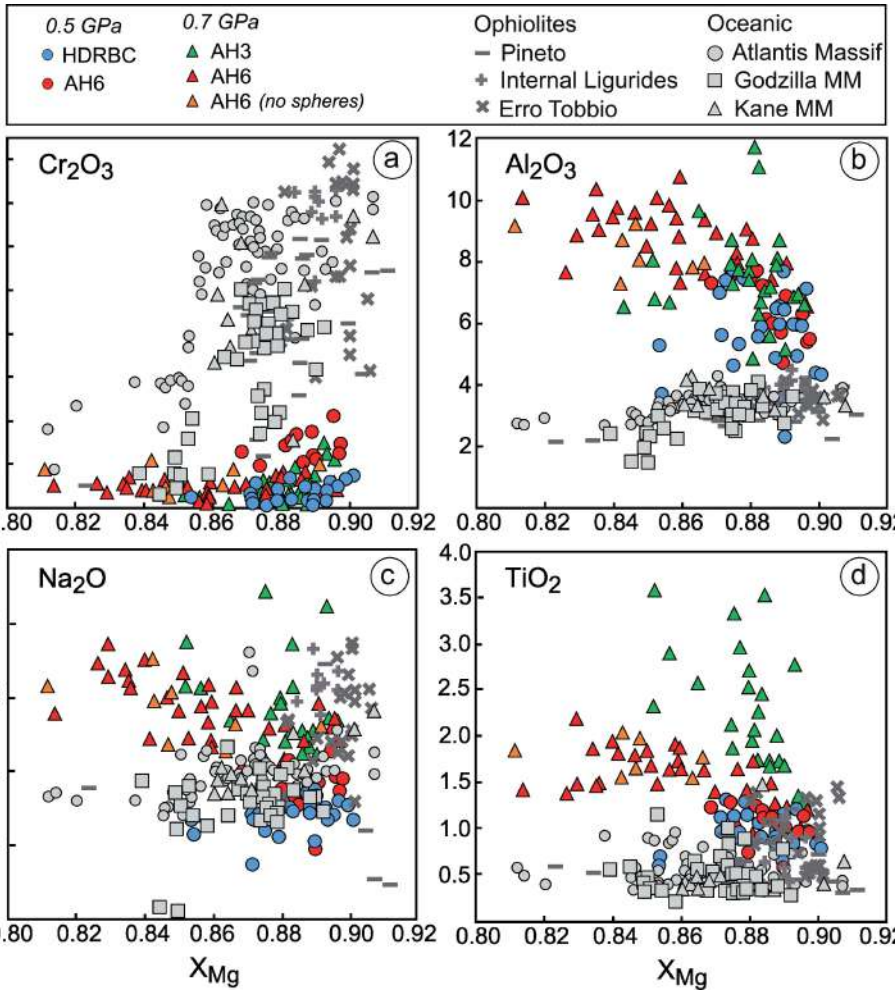
0.5 GPa
HDRBC
AH6
0.7 GPa
AH3
AH6
AH6 (no spheres)
Ophiolites
Pineto
Internal Ligurides
Erro Tobbio
Oceanic
Atlantis Massif
Godzilla MM
Kane MM
Cr2O3
a
Al2O3
b
Na2O
c
TiO2
d
XMg
XMg

Figure 7

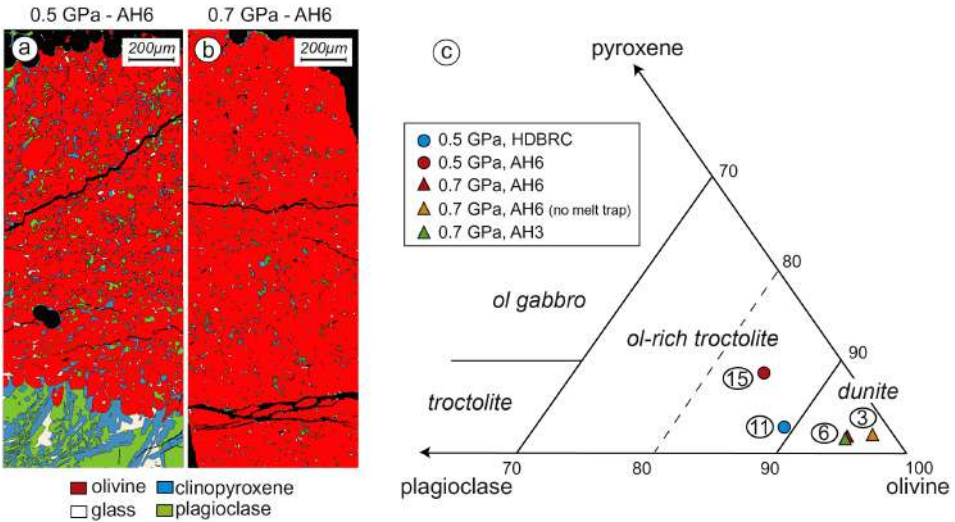
0.5 GPa - AH6
0.7 GPa - AH6
a
200µm
b
200µm
olivine
clinopyroxene
glass
plagioclase
c
pyroxene
0.5 GPa, HDBRC
0.5 GPa, AH6
0.7 GPa, AH6
0.7 GPa, AH6 (no melt trap)
0.7 GPa, AH3
70
80
90
ol gabbro
ol-rich troctolite
troctolite
dunite
15
11
6
3
70
80
90
100
plagioclase
olivine

Figure 8

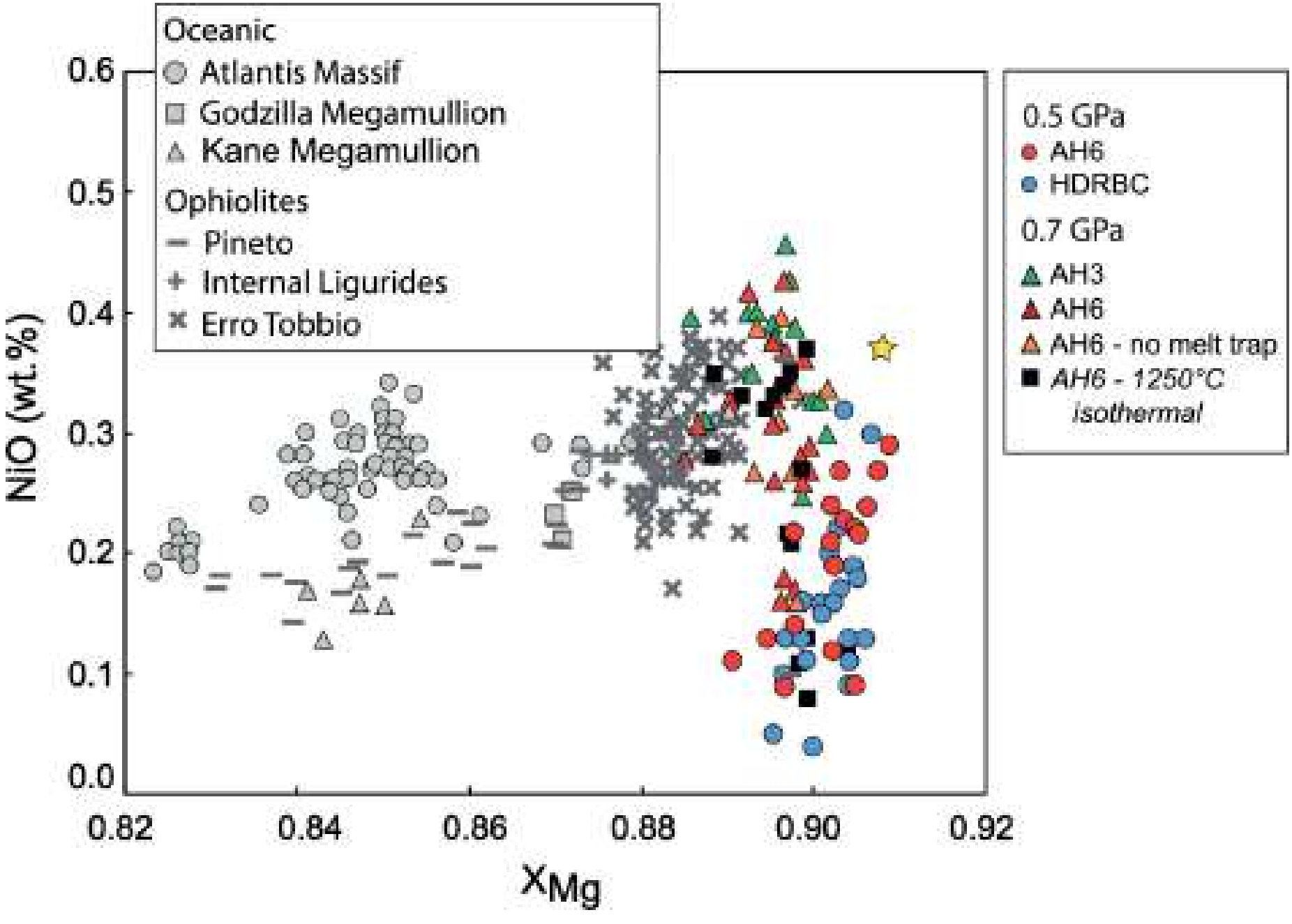
Oceanic
Atlantis Massif
Godzilla Megamullion
Kane Megamullion
Ophiolites
Pineto
Internal Ligurides
Erro Tobbio
0.5 GPa
AH6
HDRBC
0.7 GPa
AH3
AH6
AH6 - no melt trap
AH6 - 1250°C
Isothermal
NiO (wt.%)
0.6
0.5
0.4
0.3
0.2
0.1
0.0
0.82
0.84
0.86
0.88
0.90
0.92
XMg

Figure 9

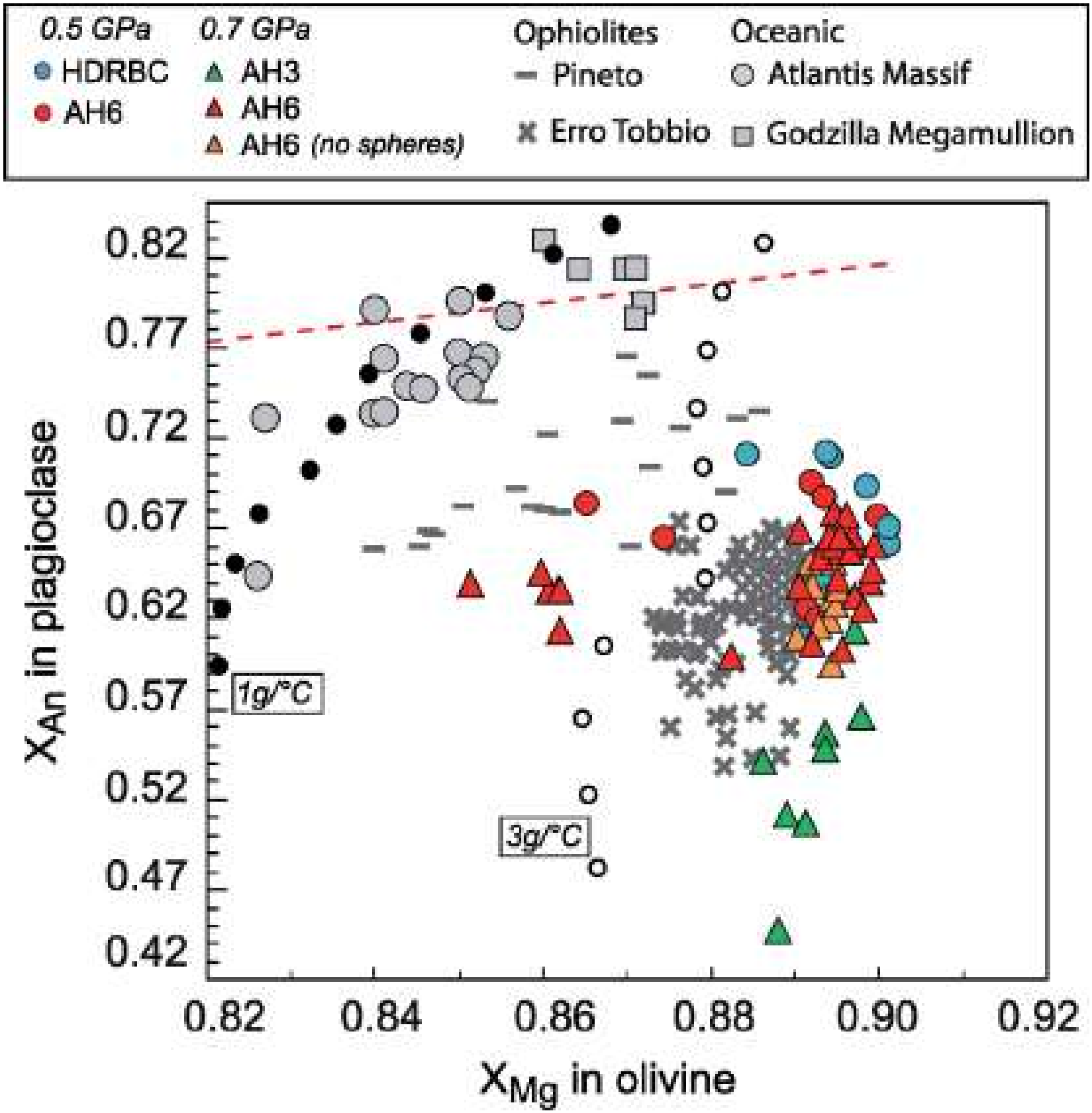
0.5 GPa
HDRBC
AH6
0.7 GPa
AH3
AH6
AH6 (no spheres)
Ophiolites
Pineto
Erro Tobbio
Oceanic
Atlantis Massif
Godzilla Megamullion
0.82
0.77
0.72
0.67
0.62
0.57
0.52
0.47
0.42
X An in plagioclase
1g/°C
3g/°C
0.82
0.84
0.86
0.88
0.90
0.92
X Mg in olivine

Figure 10